QUASISTATIC FRACTURE USING NONLINER-NONLOCAL ELASTOSTATICS WITH EXPLICIT TANGENT STIFFNESS MATRIX

A PREPRINT

Patrick Diehl
Center for Computation & Technology, Louisiana State University, Baton Rouge, LA

Robert Lipton
Department of Mathematics, Louisiana State University, Baton Rouge, LA
Center for Computation & Technology, Louisiana State University, Baton Rouge, LA

September 28, 2021

ABSTRACT

We apply a nonlinear-nonlocal field theory for numerical calculation of quasistatic fracture. The model is given by a regularized nonlinear pairwise (RNP) potential in a peridynamic formulation. The potential function is given by an explicit formula with and explicit first and second derivatives. This fact allows us to write the entries of the tangent stiffness matrix explicitly thereby saving computational costs during the assembly of the tangent stiffness matrix. We validate our approach against classical continuum mechanics for the linear elastic material behavior. In addition, we compare our approach to a state-based peridynamic model that uses standard numerical derivations to assemble the tangent stiffness matrix. The numerical experiments show that for elastic material behavior our approach agrees with both classical continuum mechanics and the state-based model. The fracture model is applied to produce a fracture simulation for a ASTM E8 like tension test. We conclude with an example of crack growth in a pre-cracked square plate. For the pre-cracked plate, we investigated *soft loading* (load in force) and *hard loading* (load in displacement). Our approach is novel in that only bond softening is used as opposed to bond breaking. For the fracture simulation we have shown that our approach works with and without initial damage for two common test problems.

1 Introduction

Peridynamic theory (PD) [63], [65], is a non-local formulation of continuum mechanics that autonomously nucleates and propagates fracture. The formulation successfully captures qualitative features seen in a range of experiments [22]. As of this writing it appears that only a few quasi static PD simulations are available [21, 32, 53, 72, 69, 7, 39, 57, 25]. For quasi static problems there is no inertia and time is represented by a load parameter. One significant reason behind the paucity of quasi-static PD simulations is the additional computational expense in going from dynamic methods with explicit time integration $\mathcal{O}(n^2)$ to a quasi- static implementation with an implicit time integration $\mathcal{O}(n^4)$, where n is the number of discrete PD nodes. The major expense here is the assembly of the tangent stiffness matrix $\mathcal{O}(n^4)$.

Several methods were proposed to speed up the time integration. Finite element approaches (FEM) for PD [10, 24, 51] were applied and found to reduce the computational costs for the assembly of the tangent stiffness matrix to $\mathcal{O}(n^3)$. For purely elastic problems Wang [70] developed a Galerkin method that exploits the matrix structure and reduces the costs of solving the matrix system from $\mathcal{O}(n^3)$ to $\mathcal{O}(n\log^2(n))$. In another direction, Chen [10] proposed a simplified model to reduce the computational costs to $\mathcal{O}(n)$ but with a reduced convergence rate of only first order for linear (FEM). Prakash [55] presents an algorithm using sparse matrices for the assembly of the tangent stiffness matrix instead a dense matrix. The sparse algorithms scaled approximately linearly with the problem size, whereas the dense matrix algorithm scales non-linearly as one would expect. The performance of the sparse implementation is compared with an adaptive dynamic relaxation scheme (ADR) in [9, 66, 39]. It is found that a speed-up factor between 12 and 22 against the ADR solve is achievable. Shiihara [62] implemented the Fire algorithm [6] which originated from molecular dynamics within the PD framework. The Fire algorithm converges about 100 time faster than the energy based relaxation method. Hu[31, 30] solved the linear equation system iterative using the GMRES algorithm [59] in conjunction with the Arnoldi process [2, 60]. Another approach to speed-up nonlocal diffusion [35] or peridynamics [34] is the convolution-based method which reduces the computational costs to $\mathcal{O}(nlog_2(n))$.

In this paper, we propose a different approach. We apply an explicit regularized nonlinear pairwise (RNP) potential [41, 47, 44] in our peridynamic formulation. The potential function is given by explicit formulas with explicit derivatives. This fact allows us to write the entries of the tangent stiffness matrix using explicit formulas, thereby saving computational costs during the assembly of the tangent stiffness matrix. In the absence of fracture, numerical simulations using our model recover linear elastostatic material behavior. We compare simulations using our approach to those using a state-based peridynamic model with standard numerical derivations to assemble the tangent stiffness matrix. The numerical experiments show that for elastic material behavior, our approach agrees with both classical elastostatic continuum mechanics and the state-based model. Next, the model is applied to a fracture simulation for an ASTM E8 like tension test. The crack initiates at the upper grip section in agreement with theory. However, the crack growth becomes unstable, and the tangent stiffness matrix ceases to be invertible due to extensive localized damage - transverse to the loading direction - that occurs after a critical load step. We conclude with an example of crack growth in a pre-cracked square plate. Here, we apply the so-called soft load, which means the load is applied using an external force. In that case the crack starts to grow, and moves forward for few mesh widths, upon reducing the load the crack grows further in a stable fashion for a few more load steps, however, beyond that even with increasingly small load steps the matrix is unstable. This numerical behavior aligns with the theory of fracture mechanics [29, 11, 58]. Next, we applied the so-called hard load, which means the load is applied in displacement. Here, we could observe stable crack growth for the pre-cracked square plate. Again, this numerical behavior aligns with the theory of fracture mechanics [3]. Our approach is novel in that only bond softening is used, as opposed to bond breaking. We demonstrate that our approach works with and without initial damage for the two common test problems treated here.

The paper is organized as follows: A brief introduction on stable and unstable crack growth is presented in Section 2. The peridynamic model and quasistatic formulation is presented in Section 3. In Section 4, we demonstrate how to obtain the entries of the tangent stiffness matrix explicitly using Taylor series. In Section 5 we describe the new algorithm used to assemble the stiffness matrix and investigate its theoretical complexity. In Section 6, we present the results of our computational experiments. Here we first display the savings in computational time using our RNP potentials versus non differential potentials. We then present the validation of the implementation and present results for the mode-I fracture experiment. Concluding remarks and directions for future work are presented in Section 7.

2 On stable and unstable crack growth

The stability of crack growth is investigated in this section from the theoretical perspective. In this section, we briefly emphasize the ingredients to explain stable and unstable crack growth using soft loading and hard loading. In soft loading the load is applied using a force and in hard loading the load is applied using displacement. One important aspect to look at for crack stability is the so-called resistance curve or R curve. In this curve, the crack resistance R is plotted with respect to the crack length l. The R curve can be determined experimentally using load in displacement as specified for example in ASTM Standard E 561 [5]. Figure 1 sketches a rising R curve (thick black line) which is common for most materials. The crack starts to grow when $G = R$ when the energy release rate G is equal to the material resistance to crack growth R. However, depending on how G varies with the crack length l the crack growth is either stable or unstable. The condition for stable crack growth reads as

$$\frac{\partial G}{\partial l} \leq \frac{\partial R}{\partial l} \tag{1}$$

and the condition for unstable crack growth reads as

$$\frac{\partial G}{\partial l} > \frac{\partial R}{\partial l}. \tag{2}$$

The simplest case is a flat R curve, which is common for brittle materials, like ceramics, where the change in G with respect to the crack length is constant [26]. Here, the common failure criterion is $G > G_c$ and the crack starts to grow if the energy release rate is larger than the critical energy release rate G_c and the crack will unstably grow.

Now we look into the crack growth stability with respect to soft load (load in force) and hard load (load ind displacement). Looking at the Equation (1) and Equation (2) the stability of crack growth depends on the change in G. Figure 1 sketches the so-called R curve in thick black with respect to the crack length l. First, we look at the soft loading, where the load is applied using a force. The lines P_1, P_2, and P_3 sketch the load subjected to the geometry. The three black dots indicate the instabilities in crack growth using the soft loading. The instability occurs since the subjected load

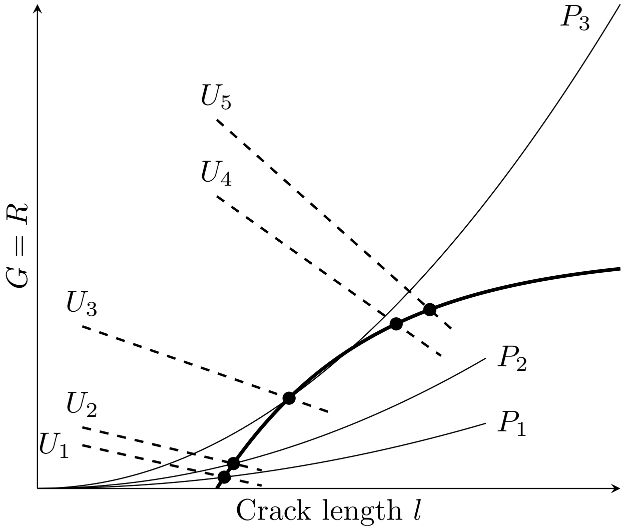

Figure 1: Sketch of a rising R curve (thick black line) which increases with the crack length l. The three thin black lines indicate soft loading, where a load P in force was applied to the geometry. The crack grow will start to grow, but will become unstable since the load is intersecting tangent to the R curve. Whereas the dotted lines show hard loading where a load U is applied in displacement to the geometry. Here the lines are interesting normal to the R curve, which indicates that the load in displacement need to be increased to let the crack develop further. This leads to Equation (1) and the crack growth tends to be more stable as in soft loading. This figure was adapted from Figure 2.11 from in[3].

in force P is tangent to the R curve. Second, we look at the hard loading, where the load is applied in displacement. The dotted lines u_1 up to u_5 show a load in displacement. Here, the lines are normal to the R curve, which means that the load in displacement needs to be increased to let the crack grow further. This leads to that hard loading tends to more stable crack growth. These theoretical aspects are observed in the numerical simulations in Section 6 where soft loading resulted in unstable crack growth and hard loading in stable crack growth. For more details about R curves and hard and soft loading we refer to Section 2 in [3].

3 Peridynamic model and quasistatic formulation

The appeal of peridynamic models is that fracture appears as an emergent phenomenon, eliminating the need for supplemental kinetic relations describing crack growth. The displacement field inside the body for points $\boldsymbol{x}$ at time t is written $\boldsymbol{u}(\boldsymbol{x}, t)$. The peridynamic model is described simply by the balance of linear momentum of the form

$$\rho \boldsymbol{u}_{tt}(\boldsymbol{x}, t) = \int_{\mathcal{H}_\epsilon(\boldsymbol{x})} \boldsymbol{f}(\boldsymbol{y}, \boldsymbol{x}) \, d\boldsymbol{y} + \boldsymbol{b}(\boldsymbol{x}, t) \tag{3}$$

where $\mathcal{H}_\epsilon(\boldsymbol{x})$ is a neighborhood of $\boldsymbol{x}$, ρ is the density, $\boldsymbol{b}$ is the body force density field, and $\boldsymbol{f}$ is a material-dependent constitutive law that represents the force density that a point $\boldsymbol{y}$ inside the neighborhood exerts on $\boldsymbol{x}$ as a result of the deformation field. The radius ϵ of the neighborhood is referred to as the *horizon*. We assume $\mathcal{H}_\epsilon(\boldsymbol{x})$ is a ball of radius ϵ centered at $\boldsymbol{x}$. Here, all points satisfy the same field equations (3). Assuming the rate of loading is slow enough that the effect of inertia term is negligible, we arrive at the quasi-static formulation which states that the body is in equilibrium at all times, hence $\boldsymbol{u}(\boldsymbol{x}, t)$ is the solution of:

$$\int_{\mathcal{H}_\epsilon(\boldsymbol{x})} \boldsymbol{f}(\boldsymbol{y}, \boldsymbol{x}) \, d\boldsymbol{y} + \boldsymbol{b}(\boldsymbol{x}, t) = \boldsymbol{0}. \tag{4}$$

Here the parameter t can now be interpreted as a load parameter.

In this work, we focus on numerical approximation of (4) when the force density $\boldsymbol{f}(\boldsymbol{y}, \boldsymbol{x})$ is given by the regularized nonlinear pairwise (RNP) model introduced in [41] and further studied in [42, 36, 37, 47, 44]. This is a two point density and the force between the two points, $\boldsymbol{f}(\boldsymbol{y}, \boldsymbol{x})$ is referred to as a bond force between $\boldsymbol{y}$ and $\boldsymbol{x}$. For small strains the nonlocal force is linearly elastic but for larger strains the force begins to soften and then approaches zero after reaching a critical strain, see Figure 2. The associated nonlocal dynamics is called *cohesive dynamics*. This type of model can be generalized to state based peridynamics, see [46].

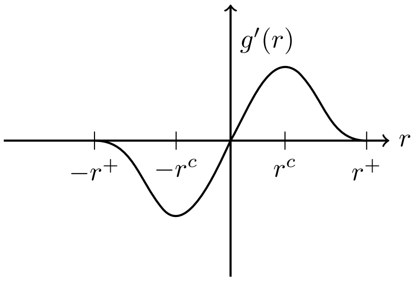

Figure 2: Cohesive force. The force goes smoothly to zero at $\pm r^+$.

The tensile strain S between two points $\boldsymbol{x}, \boldsymbol{y}$ in D along the direction $\boldsymbol{e}_{\boldsymbol{y}-\boldsymbol{x}}$ is defined as

$$S(\boldsymbol{y}, \boldsymbol{x}, \boldsymbol{u}(t)) = \frac{\boldsymbol{u}(\boldsymbol{y}, t) - \boldsymbol{u}(\boldsymbol{x}, t)}{|\boldsymbol{y} - \boldsymbol{x}|} \cdot \boldsymbol{e}_{\boldsymbol{y}-\boldsymbol{x}}, \tag{5}$$

where $\boldsymbol{e}_{\boldsymbol{y}-\boldsymbol{x}} = \frac{\boldsymbol{y}-\boldsymbol{x}}{|\boldsymbol{y}-\boldsymbol{x}|}$ is a unit vector and "$\cdot$" is the dot product. The critical strain $S_c > 0$ for which the force begins to soften is given by

$$S_c = \frac{r^c}{\sqrt{|\boldsymbol{y} - \boldsymbol{x}|}}, \tag{6}$$

and S_+ is the strain at which the force goes to zero

$$S_+ = \frac{r^+}{\sqrt{|\boldsymbol{y} - \boldsymbol{x}|}}. \tag{7}$$

The nonlocal force in the RNP model can be defined in terms of a double well potential. The bond potential is a function of the strain and is defined for all $\boldsymbol{x}, \boldsymbol{y}$ in D by

$$\mathcal{W}^\epsilon(S(\boldsymbol{y}, \boldsymbol{x}, \boldsymbol{u}(t))) = J^\epsilon(|\boldsymbol{y} - \boldsymbol{x}|) \frac{1}{\epsilon^{d+1}\omega_d |\boldsymbol{y} - \boldsymbol{x}|} g(\sqrt{|\boldsymbol{y} - \boldsymbol{x}|} S(\boldsymbol{y}, \boldsymbol{x}, \boldsymbol{u}(t))) \tag{8}$$

where $\mathcal{W}^\epsilon(S(\boldsymbol{y}, \boldsymbol{x}, \boldsymbol{u}(t)))$ is the pairwise force potential per unit length between two points $\boldsymbol{x}$ and $\boldsymbol{y}$. It is described in terms of its potential function g, given by

$$g(r) = h(r^2) \tag{9}$$

where h is concave. Here ω_d is the volume of the unit ball in dimension d, and $\epsilon^d \omega_d$ is the volume of the horizon $\mathcal{H}_\epsilon(\boldsymbol{x})$. The influence function $J^\epsilon(|\boldsymbol{y} - \boldsymbol{x}|)$ is a measure of the influence that the point $\boldsymbol{y}$ has on $\boldsymbol{x}$. Only points inside the horizon can influence $\boldsymbol{x}$ so $J^\epsilon(|\boldsymbol{y} - \boldsymbol{x}|)$ is nonzero for $|\boldsymbol{y} - \boldsymbol{x}| < \epsilon$ and zero otherwise. We take J^ϵ to be of the form: $J^\epsilon(|\boldsymbol{y} - \boldsymbol{x}|) = J(\frac{|\boldsymbol{y}-\boldsymbol{x}|}{\epsilon})$ with $J(r) = 0$ for $r \geq 1$ and $0 \leq J(r) \leq M < \infty$ for $r < 1$. One of the examples of g is:

$$g(r) = C(1 - \exp[-\beta r]) \tag{10}$$

where C, β are material dependent parameters.

In the RNP model, the bond force $\boldsymbol{f}(\boldsymbol{x}, \boldsymbol{y})$ is the derivative of the bond potential given by

$$\boldsymbol{f}(\boldsymbol{x}, \boldsymbol{y}) = 2\partial_S \mathcal{W}^\epsilon(S(\boldsymbol{y}, \boldsymbol{x}, \boldsymbol{u}(t))) \boldsymbol{e}_{\boldsymbol{y}-\boldsymbol{x}}, \tag{11}$$

where

$$\partial_S \mathcal{W}^\epsilon(S(\boldsymbol{y}, \boldsymbol{x}, \boldsymbol{u}(t))) = \frac{1}{\epsilon^{d+1}\omega_d} \frac{J^\epsilon(|\boldsymbol{y} - \boldsymbol{x}|)}{|\boldsymbol{y} - \boldsymbol{x}|} \partial_S g(\sqrt{|\boldsymbol{y} - \boldsymbol{x}|} S(\boldsymbol{y}, \boldsymbol{x}, \boldsymbol{u}(t))). \tag{12}$$

The potential energy of the motion is given by

$$PD^\epsilon(\boldsymbol{u}) = \int_D \int_{\mathcal{H}_\epsilon(\boldsymbol{x}) \cap D} |\boldsymbol{y} - \boldsymbol{x}| \mathcal{W}^\epsilon(S(\boldsymbol{y}, \boldsymbol{x}, \boldsymbol{u}(t))) \, d\boldsymbol{y} d\boldsymbol{x}, \tag{13}$$

and define the energy

$$\mathrm{E}(\boldsymbol{u}, t) = -PD^\epsilon(\boldsymbol{u}) + \int_D \boldsymbol{b} \cdot \boldsymbol{u} \, d\boldsymbol{x}.$$

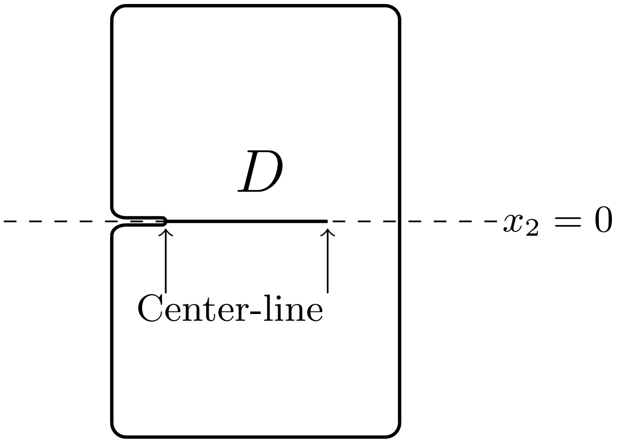

Figure 3: Failure zone center-line.

On taking the first variation of the energy we see that the stationary point is the solution of the Euler-Lagrange equation (4).

For convenience set

$$\mathcal{L}(\boldsymbol{u})(\boldsymbol{x}) = \int_{\mathcal{H}_\epsilon(\boldsymbol{x})} \boldsymbol{f}(\boldsymbol{y}, \boldsymbol{x})\, d\boldsymbol{y}. \tag{14}$$

We assume at $t = 0$ that there exists a displacement $\boldsymbol{u}_0 = \boldsymbol{u}(\boldsymbol{x}, 0)$ and body force $\boldsymbol{b}(\boldsymbol{x}, 0)$ for which the displacement is at equilibrium

$$\mathcal{L}(\boldsymbol{u}_0)(\boldsymbol{x}) + \boldsymbol{b}(\boldsymbol{x}, 0) = \boldsymbol{0}, \tag{15}$$

and the quasistatic evolution $\boldsymbol{u}(\boldsymbol{x}, t) : D \times [0, T] \to \mathbb{R}^d$ is given by

$$\mathcal{L}(\boldsymbol{u})(\boldsymbol{x}) + \boldsymbol{b}(\boldsymbol{x}, t) = \boldsymbol{0}. \tag{16}$$

for a prescribed load path $\boldsymbol{b}(\boldsymbol{x}, t) : D \times [0, T] \to \mathbb{R}^d$. Here $\boldsymbol{b}(\boldsymbol{x}, t)$ includes boundary tractions. Dirichlet boundary conditions can be applied and are described in section 6.

We propose a new numerical approach to the quasistatic evolution problem and choose a discrete load parameter with increment $\Delta > 0$. The load parameter is defined by $t = t_n = n \times \Delta$ with $0 \leq n \leq N$. At each t_n the displacement $\boldsymbol{u}(\boldsymbol{x}, t_n)$ is the solution of

$$\mathcal{L}(\boldsymbol{u})(\boldsymbol{x}) + \boldsymbol{b}(\boldsymbol{x}, t_n) = \boldsymbol{0}. \tag{17}$$

3.1 Failure Zone - Process Zone

Both pure elastic response and quasistatic fracture emerges from the model. This model can be thought of as a mesoscopic model where the model treats the fracture as a failure zone and one recovers a fracture surface by passing to the limit of vanishing horizon $\epsilon \to 0$. This has been shown for the dynamic case, where the failure zone converges to a surface as $\epsilon \to 0$ and the RNP model recovers the energy of linear elastic fracture mechanics as the peridynamic horizon goes to zero, see [41, 42]. The Kinetic relation for the RNP model converges to that of LEFM [38] and for prescribed crack paths the displacement field converges to the solution of the wave equation on time-dependent domains [43].

The failure zone represents the crack in the RNP model. It is characterized by the failure zone center-line. In an illustrative example, the failure zone center-line starts at a notch tip on the left side of the specimen and propagates into the interior. The force between two points $\boldsymbol{x}$ and $\boldsymbol{y}$ separated by the failure zone center-line is zero. The center-line is shown in figure 3 and the failure zone is the grey region in figure 4. For the boundary conditions chosen here, failure is in tension and confined to a neighborhood of the $x_2 = 0$ axis of width 2ϵ. Just in front of the failure zone is the process zone, where the force between two points $\boldsymbol{x}$ and $\boldsymbol{y}$ on either side of the $x_2 = 0$ axis is decreasing with increasing strain. At the leading edge of the crack, one sees force softening between points $\boldsymbol{x}$ and $\boldsymbol{y}$ and as the crack center-line moves forward passing between $\boldsymbol{x}$ and $\boldsymbol{y}$ the force between $\boldsymbol{x}$ and $\boldsymbol{y}$ decreases to zero, see figure 4. It needs to be stressed the failure zone and process zone emerge from the nonlocal dynamics and are not prescribed. The

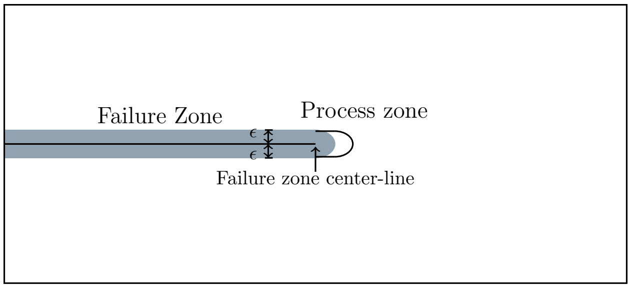

Figure 4: The failure zone is the gray shaded region and the process zone is the clear region inside the contour.

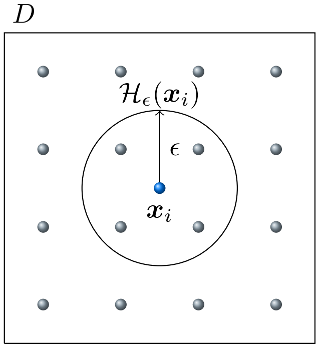

Figure 5: The material points at discrete positions $\boldsymbol{x}_i$ in the domain D in the reference configuration at time $t = 0$. For each discrete material point $\boldsymbol{x}_i$ the neighborhood $\mathcal{H}_\epsilon(\boldsymbol{x}_i) := \{j| \; |\boldsymbol{x}_j - \boldsymbol{x}_i| < \epsilon\}$ is computed. As an example, the neighborhood for the discrete node $\boldsymbol{x}_i$ is shown. The material point $\boldsymbol{x}_i$ exchanges force with all other discrete nodes within its neighborhood. Adapted from [14].

damage at each node X is given by

$$d(\boldsymbol{x}) = \max\left(\frac{S(\boldsymbol{y}, \boldsymbol{x}, \boldsymbol{u}(t))}{r^c\sqrt{|\boldsymbol{y} - \boldsymbol{x}|}}\right), \; \forall \boldsymbol{y} \in \mathcal{H}_\epsilon(\boldsymbol{x}). \tag{18}$$

When $d(\boldsymbol{X}) < 1$ the maximally stretched bonds lie below the inflection point r^c and the material is behaving elastically, for $d(\boldsymbol{X}) = 1$ the maximal bond stretch corresponds now to the strength of the material, and for $d(\boldsymbol{X}) > 1$ the collection of maximally stretched bonds have started to soften and have begun the failure process.

3.2 Discretization

To discretize the peridynamic equations of motion, a finite difference approximation is utilized. Figure 5 shows the domain D in the initial configuration at time $t = 0$. A set of mesh nodes $\{\boldsymbol{x}_i \in \mathbb{R}^d\}_{i=1}^N \subset D$ is placed in the domain D. To each of the nodes, surrounding volumes $\{V_i \in \mathbb{R}\}_{i=1}^N$ is associated. These volumes are nonoverlapping $V_i \cap V_j = \emptyset$ and recover $\sum_{i=1}^N V_i \approx |D|$ the volume of the domain D. Each node $\boldsymbol{x}_i$ interacts with all neighbors within the finite neighborhood $\mathcal{H}_\epsilon(\boldsymbol{x}_i) = \{\boldsymbol{x}_j \,|\, |\boldsymbol{x}_j - \boldsymbol{x}_i| \leq \epsilon\}$.

4 Derivation of the analytic stiffness matrix

We seek a displacement field $\boldsymbol{u}$ that satisfies the quasistatic formulation

$$\mathcal{L}(\boldsymbol{u})(\boldsymbol{x}) + \boldsymbol{b}(\boldsymbol{x}) = 0.$$

$\mathcal{L}$, see expression Equation 14, depends nonlinearly on the displacement $\boldsymbol{u}$. To make above problem tractable and implementable in a computer, we apply the Newton's iterative method which is outlined in Algorithm 1 for the soft loading case, where the load is applied via the external force density $\boldsymbol{b}$; and in Algorithm 2 for the hard loading case, where the load is applied via a prescribed displacement on an extension of the domain D.

Algorithm 1 Solver using a Newton method for the soft loading case, where the load is applied via the external force density $\boldsymbol{b}$.

```
Start with the initial guess of displacement $\boldsymbol{u}_0$
for $0 \leq k \leq N$ do
    Take $\boldsymbol{u}^k = \boldsymbol{u}^{k-1} + \Delta \boldsymbol{u}$
    Linearize $\mathcal{L}$ such that $\mathcal{L}(\boldsymbol{u}^k) = \mathcal{L}(\boldsymbol{u}^{k-1}) + H(\boldsymbol{u}^{k-1})[\Delta \boldsymbol{u}]$
    Solve for increment $\Delta \boldsymbol{u}$ using
        $H(\boldsymbol{u}^{k-1})[\Delta \boldsymbol{u}] + \mathcal{L}(\boldsymbol{u}^{k-1}) + \boldsymbol{b}(u^{k-1}) = 0. \qquad (19)$
    if $\|\boldsymbol{u}^k - \boldsymbol{u}^{k-1}\| < \delta$ then
        Exit loop
    end if
end for
```

Algorithm 2 Solver using a Newton method for the hard loading case, where the load is applied via a prescribed displacement on an extension of the domain D

```
Extend the domain and applied the prescribed displacement $\mathbf{w}$ in the extension, see Figure 6a.
Start with the initial guess of displacement $\boldsymbol{u}_0 = 0$
for $0 \leq k \leq N$ do
    Take $\boldsymbol{u}^k = \boldsymbol{u}^{k-1} + \Delta \boldsymbol{u}$
    Linearize $\mathcal{L}$ such that $\mathcal{L}(\boldsymbol{u}^k) = \mathcal{L}(\boldsymbol{u}^{k-1}) + H(\boldsymbol{u}^{k-1})[\Delta \boldsymbol{u}]$
    Solve for increment $\Delta \boldsymbol{u}$ using
        $H(\boldsymbol{u}^{k-1})[\Delta \boldsymbol{u}] + \mathcal{L}(\boldsymbol{u}^{k-1} + \mathbf{w}) = 0. \qquad (20)$
    if $\|\mathbf{w}\| - \|\boldsymbol{u}^k\| < \delta$ then
        Exit loop
    end if
end for
```

We next derive the formula for $H(\boldsymbol{u})[\boldsymbol{w}]$. Substituting Equation 11 into Equation 14, and taking $\boldsymbol{u} = \boldsymbol{u}_0 + \Delta \boldsymbol{u}$, we have

$$\begin{aligned} &\mathcal{L}(\boldsymbol{u}_0 + \Delta \boldsymbol{u})(\boldsymbol{x}) \\ &= \frac{2}{\epsilon^{d+1}\omega_d} \int_{D \cap \mathcal{H}_\epsilon(\boldsymbol{x})} \frac{J^\epsilon(|\boldsymbol{y}-\boldsymbol{x}|)}{\sqrt{|\boldsymbol{y}-\boldsymbol{x}|}} g'(\sqrt{|\boldsymbol{y}-\boldsymbol{x}|} S(\boldsymbol{y}, \boldsymbol{x}, \boldsymbol{u}_0 + \Delta \boldsymbol{u})) \boldsymbol{e}_{\boldsymbol{y}-\boldsymbol{x}} d\boldsymbol{y}, \end{aligned} \tag{21}$$

From the definition of S in Equation 5, we have

$$S(\boldsymbol{y}, \boldsymbol{x}; \boldsymbol{u}_0 + \Delta \boldsymbol{u}) = S(\boldsymbol{y}, \boldsymbol{x}; \boldsymbol{u}_0) + S(\boldsymbol{y}, \boldsymbol{x}; \Delta \boldsymbol{u}). \tag{22}$$

Let us do a Taylor expansion for the first derivative of the potential h

$$\begin{aligned} g'(\sqrt{|\boldsymbol{y}-\boldsymbol{x}|} S(\boldsymbol{y}, \boldsymbol{x}; \boldsymbol{u}_0 + \Delta \boldsymbol{u})) &= g'(\sqrt{|\boldsymbol{y}-\boldsymbol{x}|} S(\boldsymbol{y}, \boldsymbol{x}; \boldsymbol{u}_0)) \\ &\quad + g''(\sqrt{|\boldsymbol{y}-\boldsymbol{x}|} S(\boldsymbol{y}, \boldsymbol{x}; \boldsymbol{u}_0)) \sqrt{|\boldsymbol{y}-\boldsymbol{x}|} S(\boldsymbol{y}, \boldsymbol{x}; \Delta \boldsymbol{u}) \\ &\quad + O(||\Delta \boldsymbol{u}||^2). \end{aligned} \tag{23}$$

Substituting the above in Equation 21, we get

$$\begin{aligned} \mathcal{L}(\boldsymbol{u}_0 + \Delta \boldsymbol{u})(\boldsymbol{x}) &= \mathcal{L}(\boldsymbol{u}_0)(\boldsymbol{x}) \\ &\quad + \frac{2}{\epsilon^{d+1}\omega_d} \int_{D \cap \mathcal{H}_\epsilon(\boldsymbol{x})} \frac{J^\epsilon(|\boldsymbol{y}-\boldsymbol{x}|)}{\sqrt{|\boldsymbol{y}-\boldsymbol{x}|}} g''(\sqrt{|\boldsymbol{y}-\boldsymbol{x}|} S(\boldsymbol{y}, \boldsymbol{x}; \boldsymbol{u}_0)) \sqrt{|\boldsymbol{y}-\boldsymbol{x}|} S(\boldsymbol{y}, \boldsymbol{x}; \Delta \boldsymbol{u}) \boldsymbol{e}_{\boldsymbol{y}-\boldsymbol{x}} d\boldsymbol{y} \\ &\quad + O(||\Delta \boldsymbol{u}||^2). \end{aligned} \tag{24}$$

Denoting the first order term above as $H(\boldsymbol{u})[\boldsymbol{w}]$ as follows

$$H(\boldsymbol{u}_0)[\Delta \boldsymbol{u}](\boldsymbol{x}) = \frac{2}{\epsilon^{d+1}\omega_d} \int_{D \cap \mathcal{H}_\epsilon(\boldsymbol{x})} J^\epsilon(|\boldsymbol{y}-\boldsymbol{x}|) g''(\sqrt{|\boldsymbol{y}-\boldsymbol{x}|} S(\boldsymbol{y}, \boldsymbol{x}; \boldsymbol{u}_0)) S(\boldsymbol{y}, \boldsymbol{x}; \Delta \boldsymbol{u}) \boldsymbol{e}_{\boldsymbol{y}-\boldsymbol{x}} d\boldsymbol{y} \tag{25}$$

Note that $H(\boldsymbol{u}_0)[\Delta \boldsymbol{u}]$ is linear in $\Delta \boldsymbol{u}$.

Discretization of quasistatic formulation and tangent matrix The discrete approximation of Equation 19 reads

$$H(\boldsymbol{u}^{k-1})[\Delta \boldsymbol{u}](\boldsymbol{x}_i) = -\boldsymbol{b}(\boldsymbol{x}_i) - \mathcal{L}(\boldsymbol{u}^{k-1})(\boldsymbol{x}_i), \tag{26}$$

where

$$\begin{aligned} \mathcal{L}(\boldsymbol{u}^{k-1})(\boldsymbol{x}_i) &= \frac{2}{\epsilon^{d+1}\omega_d} \sum_{\substack{\boldsymbol{x}_j \in H_\epsilon(\boldsymbol{x}_i), \\ \boldsymbol{x}_j \neq \boldsymbol{x}_i}} \\ &\quad \frac{J^\epsilon(|\boldsymbol{x}_j - \boldsymbol{x}_i|)}{\sqrt{|\boldsymbol{x}_j - \boldsymbol{x}_i|}} g'(\sqrt{|\boldsymbol{x}_j - \boldsymbol{x}_i|} S(\boldsymbol{x}_j, \boldsymbol{x}_i; \boldsymbol{u}^{k-1})) \boldsymbol{e}_{\boldsymbol{x}_j - \boldsymbol{x}_i} V_j \\ H(\boldsymbol{u}^{k-1})[\Delta u](\boldsymbol{x}_i) &= \frac{2}{\epsilon^{d+1}\omega_d} \sum_{\substack{\boldsymbol{x}_j \in H_\epsilon(\boldsymbol{x}_i), \\ \boldsymbol{x}_j \neq \boldsymbol{x}_i}} \\ &\quad J^\epsilon(|\boldsymbol{x}_j - \boldsymbol{x}_i|) g''(\sqrt{|\boldsymbol{x}_j - \boldsymbol{x}_i|} S(\boldsymbol{x}_j, \boldsymbol{x}_i; \boldsymbol{u}^{k-1})) S(\boldsymbol{x}_j, \boldsymbol{x}_i; \Delta \boldsymbol{u}) \boldsymbol{e}_{\boldsymbol{x}_j - \boldsymbol{x}_i} V_j. \end{aligned} \tag{27}$$

We substitute definition of $S(\boldsymbol{x}_j, \boldsymbol{x}_i; \Delta \boldsymbol{u})$ in $H(\boldsymbol{u}^{k-1})[\Delta \boldsymbol{u}]$ to write

$$\begin{aligned} &H(\boldsymbol{u}^{k-1})[\Delta \boldsymbol{u}](\boldsymbol{x}_i) \\ &= \frac{2}{\epsilon^{d+1}\omega_d} \sum_{\substack{\boldsymbol{x}_j \in H_\epsilon(\boldsymbol{x}_i), \\ \boldsymbol{x}_j \neq \boldsymbol{x}_i}} \frac{J^\epsilon(|\boldsymbol{x}_j - \boldsymbol{x}_i|)}{|\boldsymbol{x}_j - \boldsymbol{x}_i|} g''(\sqrt{|\boldsymbol{x}_j - \boldsymbol{x}_i|} S(\boldsymbol{x}_j, \boldsymbol{x}_i; \boldsymbol{u}^{k-1})) \boldsymbol{E}_{\boldsymbol{x}_j - \boldsymbol{x}_i} (\Delta \boldsymbol{u}(\boldsymbol{x}_j) - \Delta \boldsymbol{u}(\boldsymbol{x}_i)) V_j, \end{aligned} \tag{28}$$

where

$$\boldsymbol{E}_{\boldsymbol{x}_j - \boldsymbol{x}_i} = \boldsymbol{e}_{\boldsymbol{x}_j - \boldsymbol{x}_i} \otimes \boldsymbol{e}_{\boldsymbol{x}_j - \boldsymbol{x}_i}, \tag{29}$$

is the second-order tensor. Discrete problem Equation 26 can be represented as

$$\mathbb{K}(U^{k-1}) \Delta U = F^{k-1}, \tag{30}$$

where $U^{k-1}, \Delta U, F^{k-1} = F(U^{k-1})$ are discrete displacement vector at previous iteration $k-1$, the increment of the displacement in the current iteration, and force vector. Following Equation 26, we have

$$F_i^{k-1} = F(U^{k-1})_i = -\boldsymbol{b}(\boldsymbol{x}_i) - \mathcal{L}(U^{k-1})(\boldsymbol{x}_i). \tag{31}$$

It remains to show the form of the tangent matrix $\mathbb{K}$ which depends on the solution U^{k-1} from the previous iteration. We suppress the dependence of $\mathbb{K}$ on U^{k-1}, and write

$$\mathbb{K}(\mathbf{u}) = \begin{bmatrix} \mathbb{K}_{1,1} & \mathbb{K}_{1,2} & \dots & \mathbb{K}_{1,N-1} & \mathbb{K}_{1,N} \\ \mathbb{K}_{2,1} & \mathbb{K}_{2,2} & \dots & \mathbb{K}_{2,N-1} & \mathbb{K}_{2,N} \\ \vdots & \vdots & \dots & \vdots & \vdots \\ \vdots & \vdots & \dots & \vdots & \vdots \\ \vdots & \vdots & \dots & \vdots & \vdots \\ \mathbb{K}_{N-1,1} & \mathbb{K}_{N,2} & \cdots & \mathbb{K}_{N-1,N-1} & \mathbb{K}_{N,N-1} \\ \mathbb{K}_{N,1} & \mathbb{K}_{N,2} & \cdots & \mathbb{K}_{N-1,N} & \mathbb{K}_{N,N} \end{bmatrix}, \tag{32}$$

where each entry $\mathbb{K}_{ij}$ is a $d \times d$ matrix where $d = 1, 2, 3$ is the dimension of the problem. From Equation 28, we have

$$\mathbb{K}_{ij} = \begin{cases} \boldsymbol{A}_{ij}, & \text{if } i \neq j, \\ \sum_{\substack{\boldsymbol{x}_k \in \mathcal{H}_\epsilon(\boldsymbol{x}_k), \\ \boldsymbol{x}_j \neq \boldsymbol{x}_i}} \boldsymbol{A}_{ik}, & \text{if } i = j, \end{cases} \tag{33}$$

where second order tensor $\boldsymbol{A}_{ij}$ is given by

$$\boldsymbol{A}_{ij} \equiv \boldsymbol{A}_{ij}(\boldsymbol{u}^{k-1}) = \frac{2}{\epsilon^{d+1}\omega_d} \frac{J^\epsilon(|\boldsymbol{x}_j - \boldsymbol{x}_i|)}{|\boldsymbol{x}_j - \boldsymbol{x}_i|} g''(\sqrt{|\boldsymbol{x}_j - \boldsymbol{x}_i|} S(\boldsymbol{x}_j, \boldsymbol{x}_i; \boldsymbol{u}^{k-1})) \otimes \boldsymbol{E}_{\boldsymbol{x}_j - \boldsymbol{x}_i} V_j, \tag{34}$$

when $i \neq j$, and $\boldsymbol{A}_{ii} = \boldsymbol{0}$. Here by the notation $S(\boldsymbol{x}_j, \boldsymbol{x}_i; \boldsymbol{u}^{k-1})$ we mean

$$S(\boldsymbol{x}_j, \boldsymbol{x}_i; \boldsymbol{u}^{k-1}) = \frac{\boldsymbol{u}_j^{k-1} - \boldsymbol{u}_i^{k-1}}{|\boldsymbol{x}_j - \boldsymbol{x}_i|} \cdot \frac{\boldsymbol{x}_j - \boldsymbol{x}_i}{|\boldsymbol{x}_j - \boldsymbol{x}_i|}, \tag{35}$$

for discrete problems. Note, that the same approach can be used to derive the analytic stiffness for the state-based RNP model [45] with some additional linearization of the hydro-static force.

Algorithm 3 Solver using a Newton method for the soft loading case, where the load is applied via the external force density $\boldsymbol{b}$.

```
 1: Define the external force density $b$, tolerance $\delta$, and perturbation $\tau$
 2: Guess the initial displacement $\mathbf{u}_0$
 3: Compute the residual $r = \|\mathbf{F}\|$ //Equation (31)
 4: while $r \geq \delta$ do
 5:     Assemble the tangent stiffness matrix $\mathbb{K}(\mathbf{u}) \in \mathbb{R}^{d \cdot N \times d \cdot N}$ //Equation (34)
 6:     Remove all columns/rows in $\mathbb{K}$ for nodes with prescribed zero displacement (clamped nodes)
 7:     Remove all entries in $\mathbf{F}$ for nodes with prescribed zero displacement (clamped nodes)
 8:     Solve the reduced system $\mathbb{K}\Delta\mathbf{u} = \mathbf{F}$ // Equation (19)
 9:     $\boldsymbol{u}+ = \Delta u$
10:     $r = \|\mathbf{F}\|$
11: end while
```

5 Algorithm

The algorithm for solving the system $\mathbb{K}(u)x = F$ is similar to the one described in [20, 48] using a Newton method, see Algorithm 3. Note that using a generic peridynamic material model, assembling the tangent stiffness matrix, see Line 5, can become computationally expensive since the entries are approximated using numerical schemes, *e.g.* central differences,

$$\mathbb{K}_{ij}(u) \approx \frac{\mathcal{L}^T(u+\epsilon)(x_i) - \mathcal{L}^T(u-\epsilon)(x_i)}{2\tau} \tag{36}$$

by perturbation the displacement. One is refereed to [8] where a comparison of different methods are given. These include automatic differentiation, central difference scheme approach, finite difference scheme approach, and the complex step scheme [49, 50], for calculating tangent stiffness matrices in a massively parallel fashion. The relative accuracy of these schemes for computing the tangent stiffness matrix can be found in [8]. The perturbation approach requires the PD forces to be evaluated for a perturbed displacement $u \pm \tau$ over all directions, which is only computationally feasible in one dimension. For higher dimensions or numerous discrete nodes, the computational costs increase heavily, since the theoretical complexity of the algorithm is $\mathcal{O}(n^4)$. Meaning that for all n nodes the perturbed forces for all n neighbors have to be computed. Since the evaluation of the force costs n^2 operations, we have $n^2(d \cdot n^2 + d \cdot n^2)$ operations in total. On the other hand, for the RNP softening model the entries of the tangent stiffness matrix can be computed without perturbing the displacement of each node in all directions using Equation (33). Hence, the evaluation of the perturbed forces is not needed anymore and this reduces the computational cost for the RNP model to $\mathcal{O}(n^3)$.

5.1 Soft loading

Algorithm 3 sketches the solver for the bond-based softening model for the soft loading case, where the load is applied via the external force density $\boldsymbol{b}$. The solver needs the external force density $\mathbf{b}$, the tolerance δ, and the perturbation τ. A guess for the initial displacement can be zero or some small perturbation in the size of τ. The initial guess of the displacement is used to compute the residual using Equation (31) and if the residual $r < \delta$ is smaller than the tolerance the initial guess is the solution. If not, iteration of Newton steps are done to get the solution of the displacement until the residual r is less than the tolerance δ. The tangent stiffness matrix is assembled using Equation (33). To avoid a singular matrix, all entries of the stiffness matrix and the force vector are removed in Line 6 and Line 7. After that, the reduced system is solved. Note that this is just a single Newton iteration and for each successive load step, the Algorithm 3 is repeated with $\boldsymbol{u}$ from the previous load step as the current initial guess $\boldsymbol{u}_0$ and a larger external load $\boldsymbol{u}$ as shown in Algorithm 1. These steps are not shown in the discrete algorithm for simplification.

5.2 Hard loading

Algorithm 4 outlines the solver used for the bond-based softening model for the hard loading case, where the load is applied via the displacement $\boldsymbol{u}$ instead of the external force $\boldsymbol{b}$ as in the soft loading. To apply the load in displacement, the domain D is extended with a layer of $\pm\delta$ in y-direction at the top $D^{+\epsilon}$ and bottom $D^{-\epsilon}$, respectively. Note that the extension of the domain to apply boundary conditions within peridynamics was applied in the following references [56, 64, 23, 1, 27, 52, 28]. Figure 6a shows the reference configuration of the domain D. A positive load displacement $+u$ is applied to the upper extension $D^{+\epsilon}$. A negative load displacement $-u$ is applied to the lower extension $D^{-\epsilon}$. The algorithm uses the tolerance δ and the perturbation τ as input. In Line 2 the reference

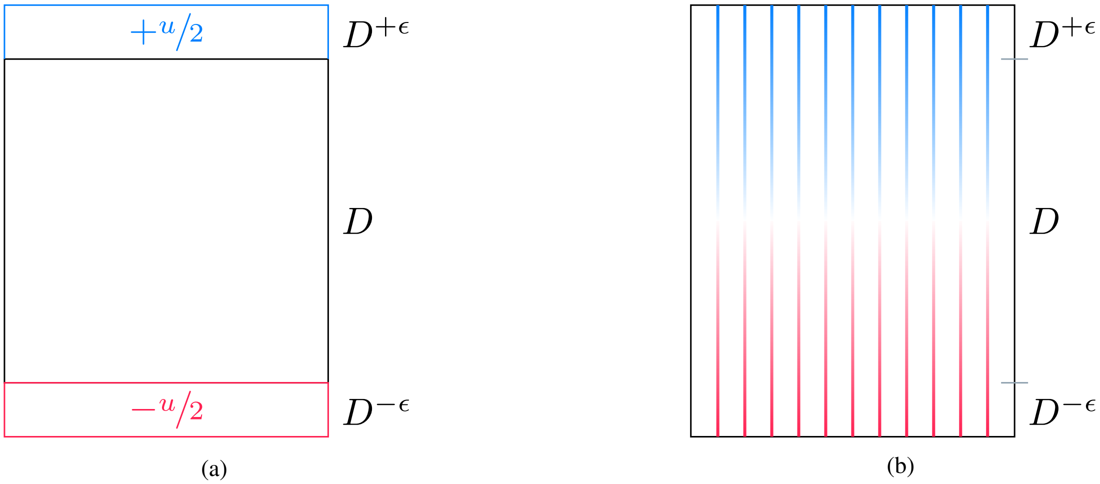

Figure 6: Extended domain for the hard loading: (a) reference configuration D with the extension $D^{+\epsilon}$ and $D^{-\epsilon}$ to apply the load in displacement $\mathbf{w}$. In this example, the assumption is made that a positive load in displacement is applied within the top extension and a negative load in displacement in the upper extension. (b) sketch of the prescribed displacement $\mathbf{w}$ in y-direction and all values in the x-direction are zero. Here, the prescribed load in displacement is applied to the extension $D^{+\epsilon}$ and $D^{-\epsilon}$. To avoid high damage concentration at the interface of the extension and the domain, the prescribed displacement needs to be extended to the reference configuration D.

configuration is extended by a layer of horizon size $\pm\epsilon$ and additional discrete PD nodes with the same nodal spacing are placed in the extension area. In Line 3 the initial displacement field $\boldsymbol{u}_0$ in the extended domain is guessed. A guess for the initial displacement can be zero or some small perturbation in the size of τ. In Line 4 the prescribed displacement is initialized. Here, the prescribed load in displacement is applied to the extension $D^{+\epsilon}$ and $D^{-\epsilon}$. For example, a constant displacement is applied to all discrete PD nodes in the extension. To avoid high damage concentration at the interface of the extension and the domain, the prescribed displacement needs to be extended to the reference configuration D. Figure 6b sketches some example field of the prescribed displacement $\mathbf{w}$ in y-direction and all values in the x-direction are zero. The displacement value is $+u/2$ and $-u/2$ in the extension and decays linearly to zero until reaching the middle of the plate. For this method, the displacement to be found $\boldsymbol{u}$ is determined by iteration so that the residual r defined by

$$r = \left(\|\mathbf{w}^{D^{+\epsilon}}\| + \|\mathbf{w}^{D^{-\epsilon}}\|\right) - \left(\|\mathbf{u}^{D^{+\epsilon}}\| + \|\mathbf{u}^{D^{-\epsilon}}\|\right), \tag{37}$$

satisfies $r < \delta$. Note that the evaluation of the residual depends on the chosen prescribed displacement $\mathbf{w}$ and in this case we assure that the prescribed displacement in the extension matches the displacement solved in the Newton iteration of the current load step. Note that at this stage, the residual r is computed using the initial guess $\boldsymbol{u}_0$. If the initial guess of the displacement is not smaller as the tolerance δ a set of Newton iterations are started until the solution satisfies the tolerance, see Line 6. Inside the `while` loop all steps are identical to the ones for the soft loading (Algorithm 3), except that the force $\mathbf{F} = \mathcal{L}(\boldsymbol{u} + \mathbf{w})$ in Line 7 is evaluated differently. Note that the all fields, *e.g.* force, displacements, and damage, need to be extended and in the tangent stiffness matrix has a larger size of $m = \epsilon/h$.

6 Numerical examples

6.1 Linear elasticity

In this section, we validate our approach against classical continuum mechanics for the linear regime of the potential in Figure 2. Note that there is no damage involved since the strain is less than critical, given by the inflection point r^c. These simulations are necessary to show that our approach recovers linear elasticity and gets results comparable to the approach using the numerical differentiation.

6.1.1 One-dimensional

For the one-dimensional case, the strain ϵ_{CCM} from classical continuum mechanics (CCM) is recovered. The stress σ is defined as $\sigma = E \cdot \epsilon$ where E is the material's Young's modulus. The relation of Force F and stress

Algorithm 4 Solver using a Newton method for the hard loading case, where the load is applied using a prescribed displacement $\boldsymbol{u}$ on an extension of the domain D of $\pm\epsilon$.

```
Define the tolerance $\delta$, the load in displacement $\pm w$, and perturbation $\tau$
Extend the domain $D$ by a layer of horizon size $\pm\epsilon$ //see Figure 6a.
Guess the initial displacement $\mathbf{u}_0$
Initialize the prescribed displacement $\mathbf{w}$
Compute the residual $r = \left(\|\mathbf{w}^{D^{+\epsilon}}\| + \|\mathbf{w}^{D^{-\epsilon}}\|\right) - \left(\|\mathbf{u}_0^{D^{+\epsilon}}\| + \|\mathbf{u}_0^{D^{-\epsilon}}\|\right)$ //see Equation 37
while $r \geq \delta$ do
    Compute $\mathbf{F} = \mathcal{L}(\boldsymbol{u} + \mathbf{w})$
    Assemble the tangent stiffness matrix $\mathbb{K}(\mathbf{u}) \in \mathbb{R}^{d\cdot(N+\epsilon/h)\times d\cdot(N+\epsilon/h)}$ //Equation (34)
    Remove all columns/rows in $\mathbb{K}$ for nodes with prescribed zero displacement (clamped nodes)
    Remove all entries in $\mathbf{F}$ for nodes with prescribed displacement (clamped nodes)
    Solve the reduced system $\mathbb{K}\Delta\mathbf{u} = \mathbf{F}$ // Equation (20)
    $\boldsymbol{u} += \Delta u$
    $r = \left(\|\mathbf{w}^{D^{+\epsilon}}\| + \|\mathbf{w}^{D^{-\epsilon}}\|\right) - \left(\|\mathbf{u}^{D^{+\epsilon}}\| + \|\mathbf{u}^{D^{-\epsilon}}\|\right)$ //see Equation 37
end while
```

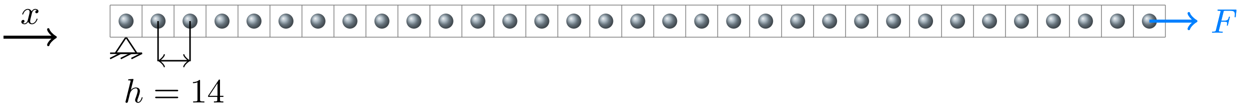

Figure 7: Sketch of the one dimensional bar benchmark test. The node on the left-hand side is clamped with respect to displacement ($u = 0$). A force F is applied on the node at the right-hand side. Adapted from [17].

reads as $\sigma = {}^{F}/_{A}$ with A as the area of the cross-section. Applying these two relations, the strain is obtained by $\boldsymbol{\epsilon} = {}^{\boldsymbol{\sigma}}/\boldsymbol{E} = {}^{\boldsymbol{F}}/(\boldsymbol{A}\cdot\boldsymbol{E})$. Assuming a force F of 40N, a cross-section of 1m^2, and a Young's modulus E of 40GPa, the strain reads as $\boldsymbol{\epsilon_{CCM}} = 1 \times 10^{-8}$.

Figure 7 sketches the geometry for the one-dimensional model problem, which is used to recover the strain from classical continuum mechanics. The node on the left-hand side is clamped with respect to displacement. A load force is applied to the first node. The length of the bar is 16m. We chose $\delta = 3 \cdot h$ with $h = 1/4$, a length $L = 16$ and the tolerance was set to $\delta = 1 \times 10^{-11}$. To determine the bond-based material properties C and β in Equation (10), we used the relation $E = C \cdot \beta$. Since, we are interested in the linear elastic region of the potential, we can set $\beta = 1$ and thus $E = C = 40\text{GPa}$. For more details on the energy equivalence for the one-dimensional bond-based softening model, we refer to [36].

For the global strain we get, $\boldsymbol{\epsilon} = 1.01 \times 10^{-8}$ which is close to the strain predicted by classical continuum mechanics $\boldsymbol{\epsilon_{CCM}} = 1 \times 10^{-8}$. As a second validation, the same discretized bar was simulated using the Silling's state based model [65] and the assembly of the tangent stiffness matrix using the numerical approximation of derivative as in [48]. In that case the predicted strain is $\boldsymbol{\epsilon} = 1.0 \times 10^{-8}$ using the author's C++ code [20]. The python code finished in 1.04s (24 iterations) using the presented approach, and the numerical approximation of the tangent stiffness matrix took 3.71s (31 iterations).

6.1.2 Two-dimensional

For the two-dimensional problem, the geometry in Figure 8, which is a square plate of $W = 16\,\text{mm}$ times $L = 16\,\text{mm}$, is used. The nodes on the right-hand side are clamped in displacement ($u_x = u_y = 0$). A body force $F = -40\text{N}$ is applied on the first line of nodes on the left-hand side. The nodal spacing is chosen as $h = 0.1$ and the horizon is $\delta = 5h$. The material properties are chosen as Young's modulus $E = 4000$, Poisson's ratio $\nu = {}^{1}/_{3}$, and Energy release rate $G = 500$.

To validate our assembly of the stiffness matrix, we use the solution from classical continuum mechanics, see [20], derived by using the Airy stress function [61]. The following equations show the displacement obtained by classical

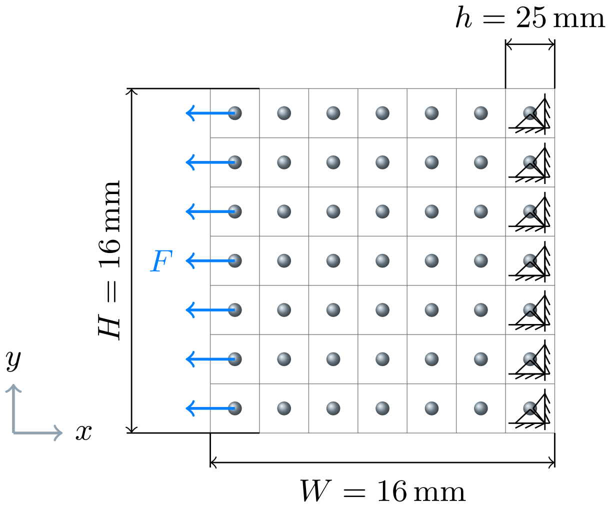

Figure 8: Sketch of the two-dimensional square plate for benchmark. The displacement of the last layer of nodes is fixed in both directions. An external force in negative x-direction is applied to the first layer of nodes. Adapted from [16].

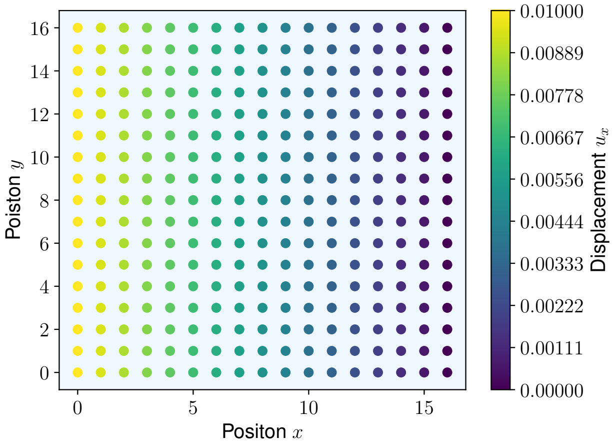

Figure 9: Displacement u_x (a) and u_y (b) at the nodes obtained by classical continuum mechanics from Equation (38).

continuum mechanics

$$. \tag{38}$$

Figure 9 shows the solution of the displacement fields from Equation (38). The bond-based material parameters C and β in Equation (10) can be related to classical continuum mechanics as follows [12]

$$C = \frac{16}{6}\frac{K_{\mathrm{IC}}^2}{E}, \tag{39}$$

$$\beta = \frac{20\mu}{\beta}. \tag{40}$$

Figure 10a shows the displacement u_x obtained with our approach using a tolerance $\delta = 1 \times 10^{-6}$. The error with respect to CCM is overestimated by 13.7%. Figure 10b shows the displacement u_x obtained by assemble of the tangent stiffens matrix using the numerical approximation of derivative as in [48]. Note that the state-based model of Silling [65] instead of a bond-based model was used, however, the tolerance $\delta = 1 \times 10^{-6}$ was the same. Here, there is no error with respect to CCM. Note that one would have to do a convergence study for both quasi-static methods by varying the nodal spacing h and the horizon δ. However, this is out of the scope of the paper, since the focus of

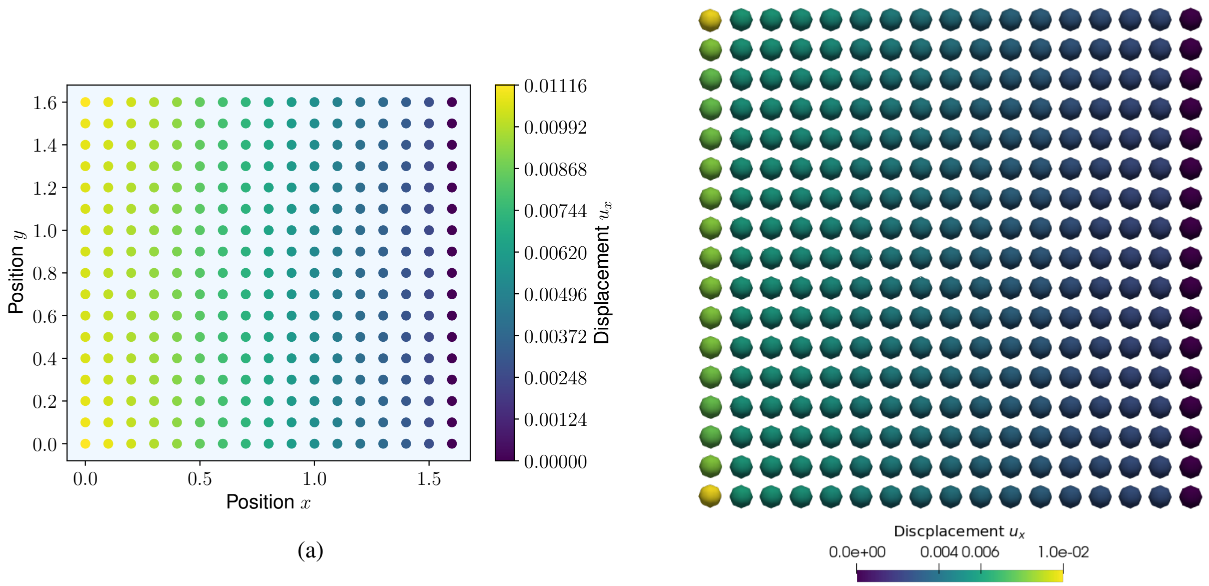

(a)

(b)

Figure 10: Displacement u_x (a) obtained by our approach using a bond-based peridynamic model and u_x (b) obtained using the numerical derivation for the stiffness matrix and a state-based model using the authors C++ code. Adapted from [18].

the paper is the analytic assembly of the stiffness matrix and validation of the approach to CCM and the approach to assemble the stiffness matrix using the numerical approximation of the derivative.

The computation time for our approach employing the analytic stiffness matrix took 238 minutes using the prototype Python code with one CPU while for the computationally assembled stiffness matrix approach we used the author's C++ code, and it took 191 minutes using five CPUs. Thus, for this example, the analytic approach seems to be far more efficient than the standard numerical perturbation approach.

6.2 Damage

Previously, we validated our approach against classical continuum mechanics and now, we will show the performance of our method for fracture simulations. First, we investigate the influence of softening bonds on the condition number of the tangent stiffness matrix in Section 6.2.1. An ASTM E8 like tensile test is done to observe crack initiation in Section 6.2.2. Last, a notched square plate is used as an example for crack growth from a pre-crack in Section 6.2.3 for the soft loading and in Section 6.2.4 for the hard loading, respectively.

6.2.1 User controlled damage

To study the influence of broken bonds on the matrix's condition number, the two-dimensional model problem in Section 6.1.2 is employed without the applied boundary conditions. A precrack from (0,0.8) to (0.8,0.8) is introduced. The precrack is modeled by excluding all peridynamic bonds that intersect this line from the neighborhood $B_\delta(x)$. Figure 11a shows the grid with the initial crack and all discrete PD nodes are colored with the number of neighbors. To analyze the influence of softening bonds on the condition number of the stiffness matrix K, bonds adjacent to the pre-crack crack are artificially softened to zero for three different scenarios: 1) the crack grows each time step by $^1/_2$ of the mesh size h, 2) grows at each step by exactly the mesh size, and 3) grows at each time step by $1.5\ h$. Figure 11 shows the artificial crack growth for the second case. Figure 12 shows the condition number $con(K)$ of the stiffness matrix K for all three cases. The condition number $con(K) = {}^{|K|_{L_2}}/_{|K^{-1}|_{L_2}}$ was obtained using Numpy where the method described in [40] was implemented. For all three cases, we see that the condition number increases linearly per iteration. However, even for the fully cracked plate, the condition number is not increasing too much.

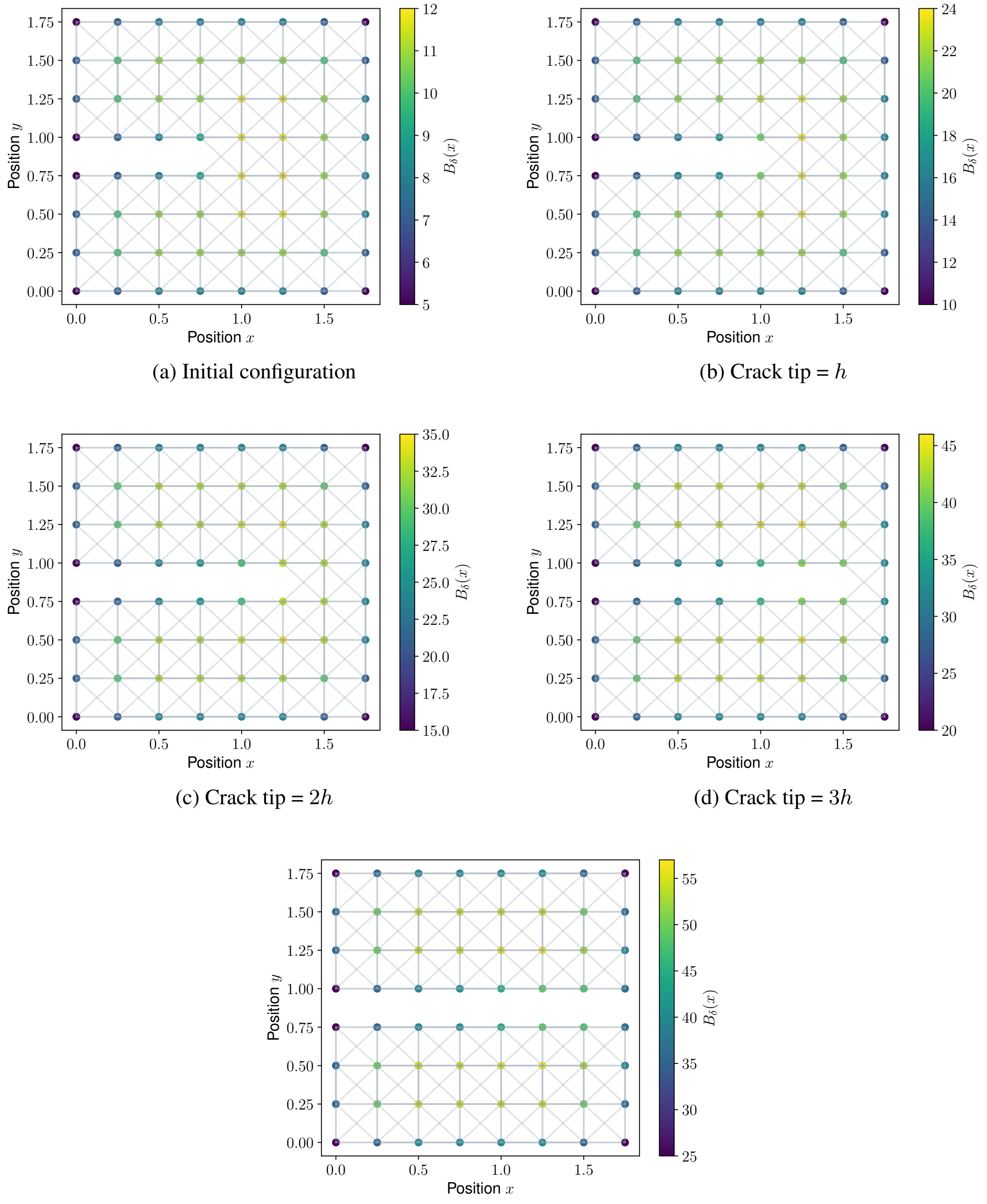

(a) Initial configuration

(b) Crack tip = h

(c) Crack tip = $2h$

(d) Crack tip = $3h$

(e) Crack tip = $4h$

Figure 11: The initial configuration of the plate with the initial crack (a). The consecutive images show the artificial grown crack, where the crack growth was controlled by softening all bonds along the initial crack. In the first iteration (b) the crack tip grows for one mesh width h. In the second iteration (c) for $2h$. In the third iteration (d) for $4h$. And in the last iteration, the plate is completely broken (e). The resulting condition number $con(K)$ for each iteration is shown in Figure 12.

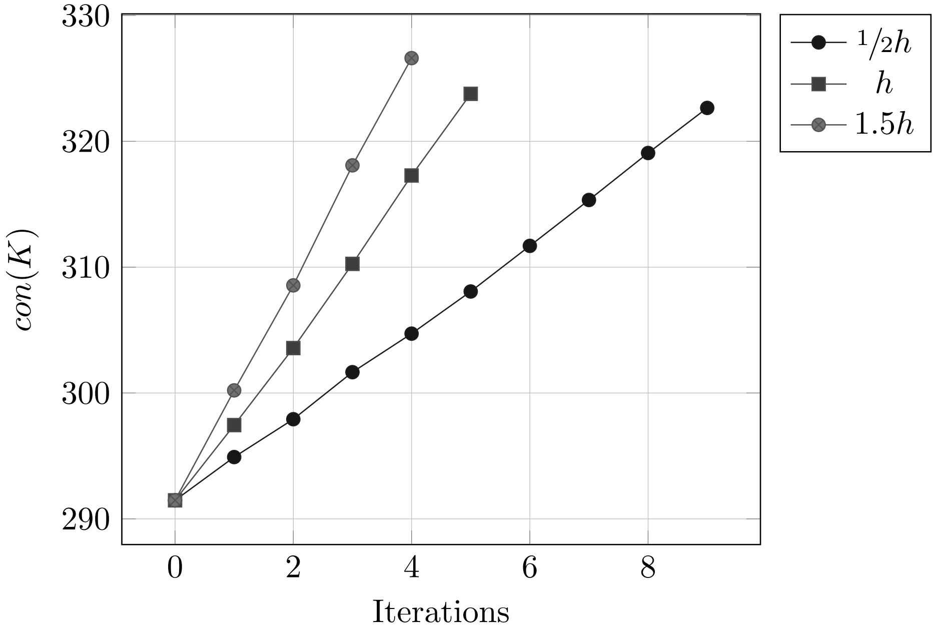

Figure 12: The condition number $con(K)$ of the tangent stiffness matrix K with respect to the crack growth. The initial configuration of the half-cracked square plate is shown in Figure 11a. At iteration zero, the condition number was computed for this configuration. To analyze the influence of soften bonds to the condition number of the stiffness matrix K, bonds along the initial crack are artificial soften to zero for three cases: 1) the crack grows $^1/_2$ of the mesh size h, 2) grows the mesh size, and 3) grows $1.5h$ per iteration.

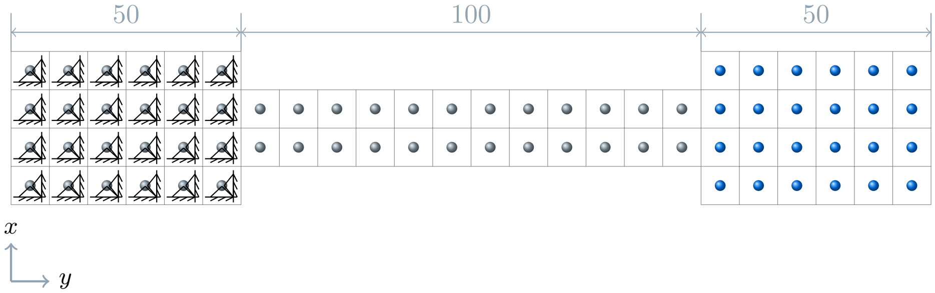

Figure 13: Sketch of the ASTM ES like tensile specimen. The green nodes. Note that we rotated the specimen by 90° and we used metric units. The nodes within the left-hand side are clamped in x-direction and y-direction. On the blue colored nodes a force of 4×10^6N is applied. Note that we apply a force density in peridynamic by dividing the force by the area of the clamped region. Adapted from [13].

6.2.2 Crack initiation for tensile testing with soft loading)

In the first two model problems, we focused on linear elasticity to showcase that our approach can reproduce the results where the cohesive force in Figure 2 stays in the linear regime. Note that these steps are necessary to validate this model, however, the interesting aspect of this approach is the part where the crack starts to initiate or grow. To showcase our approach, we now recover this important feature of peridynamics numerically. We use a flat test specimen for a tensile test according to standard *ASTM E8* [4]. Figure 13 shows the simplified geometry of the flat test specimen. Note that we rotated the specimen by 90° and we used metric units. The green colored nodes are clamped in x-direction and y-direction. On the blue colored nodes, a force of 4×10^6N is applied. Note that we apply a force density in peridynamics by dividing the force by the area of the clamped region. The nodal spacing h is set to $1\mathrm{mm}$ and the horizon δ is set to $4h$. The solver tolerance δ is set to 1×10^{-6}. For material properties, we chose C =3×10^8 and β =0.1. Note that the same model was utilized in [12] for a tensile test with explicit time integration.

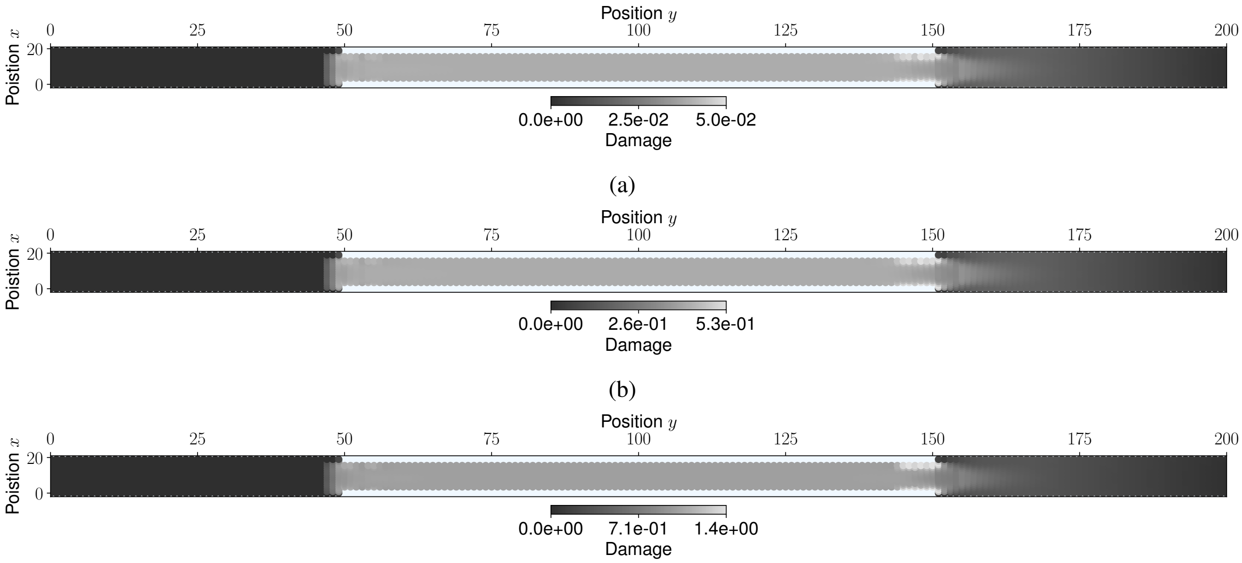

(a)

(b)

(c)

Figure 14: Damage for soft loading at the discrete PD nodes (black = undamaged and gray = damaged) for the following loading steps: (a) after the first load step, (b) after 10 load steps, and (c) after 20 load steps. Note that the damage is plotted with respect to the reference configuration D.

Figure 15 shows the evolution of the damage in the tensile specimen. Figure 14a shows the damage after one load step. Figure 14b shows the damage after 50% of the load steps. Figure 14c shows the last load step before the analytic stiffness matrix becomes singular. We tried to continue beyond the last load step using smaller load steps, however, the matrix remained unstable. This behavior of unstable crack growth is depicted in the R curve in Figure 1. Once a load which intersects the R Curve tangential is reached, for example P_3 in Figure 1, the crack growth will remain unstable while increasing the load in force. However, one can find some smaller loads in force, for example P_1 and P_2, where the crack would grow for a small length l. For more details about soft loading and R curves, we refer to [3]. However, the crack initiation's location is near to the upper grip section, which is the location where the crack should initiate. Figure 15 shows the displacement in y direction for the same load steps.

6.2.3 Pre-cracked plate with soft loading

Figure 16 shows a sketch of the precracked square plate (5×5) with an initial crack of length 7.5. All nodes within the lower and upper right-hand side square of horizon size δ are clamped in both directions. All nodes within the lower and upper left-hand side square of horizon size $\delta \times 13\delta$ are loaded with the force of $\pm 4 \times 10^6$N in y-direction. The load in force refers to the so-called soft loading in the theory of fracture mechanics. The nodal spacing h was 0.2 and the horizon δ was $4 \cdot h = 0.8$. The tolerance was set to $\delta = 1 \times 10^{-5}$. All bonds between the PD nodes crossing the initial crack line were removed from the neighborhood $H_\epsilon(\boldsymbol{x}_i)$. As material properties, we chose C =3×10^8 and β =0.1.

First, we look into the damage field while the bond stretch is still in the linear regime, see Figure 17. Note that the damage is plotted with respect to the reference configuration D. The black line indicates the initial crack, and all bonds intersecting this line are initially broken. The color map is chosen such that dark blue indicates no damage, light red indicates crack growth started, and dark red indicates that the bonds are fully softened to zero. The damage after one load step (Figure 22a) with $F_1 = \pm 4 \times 10^6$N some bonds are stretched up to 1.1% to the inflection point r^c before softening starts, and we can not see the damage yet. The damage after six load steps (Figure 17b) with $F_6 = \pm 4 \times 10^6$N and the bonds are stretched around 7.2% close to the inflection point r^c, but are still in the linear regime. The damage is localized around the tip of the initial crack.

Second, we look at the damage while the bond stretch started to soften, but the crack growth has not started yet, see Figure 18. The damage field after nine load steps (Figure 18a) with $F_9 = 36 \times 10^6$N shows that first bond stretches are at 140% and exceeding the inflection point r^c and are softening. Here, the damage is still localized in a layer of horizon size δ at the tip of the initial crack. The damage after eleven load steps (Figure 18b) with $F_{11} = 44 \times 10^6$N

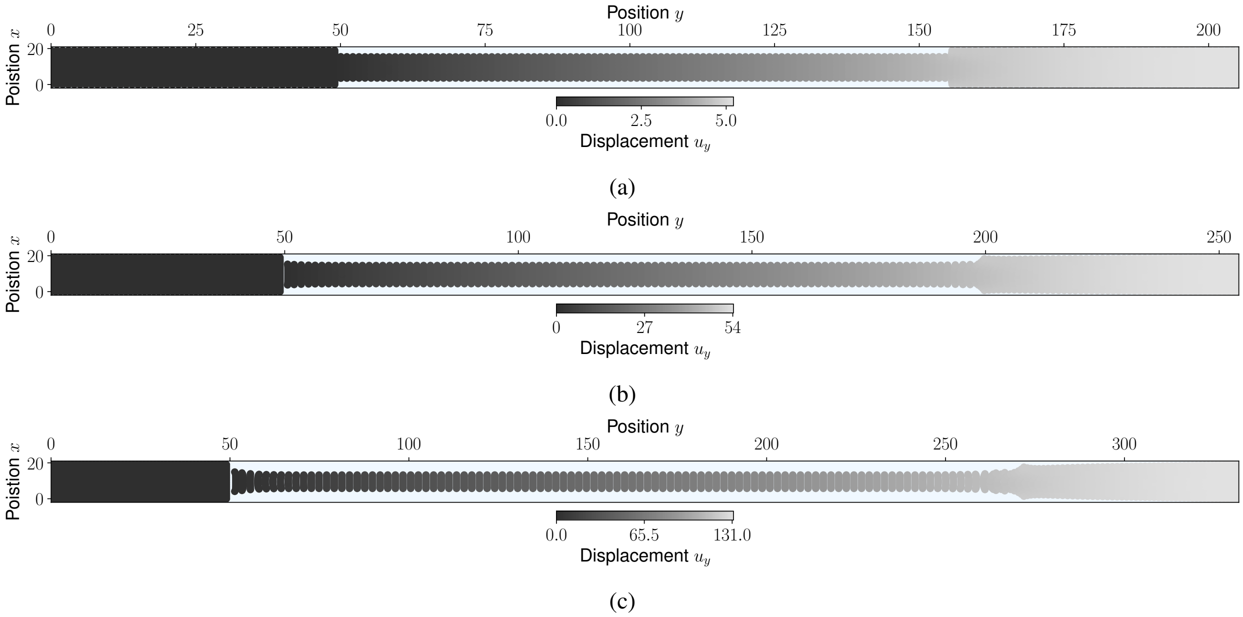

Figure 15: Displacement u_y for soft loading at the discrete PD nodes (black = 0 and gray = $max(u_y)$) for following loading steps: (a) after the first load step, (b) after 10 load steps, and (c) after 20 load steps.

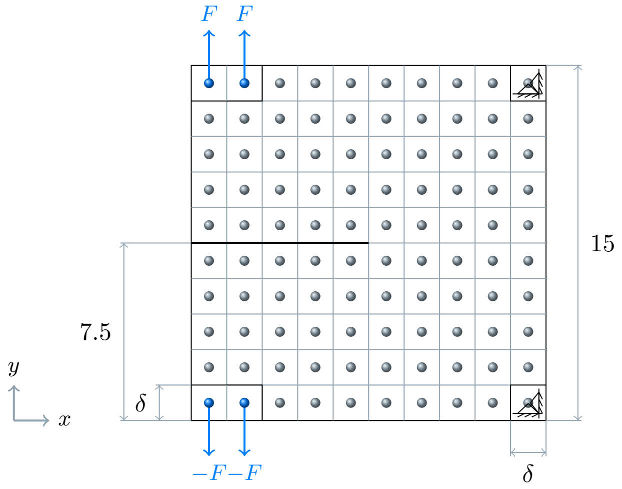

Figure 16: Sketch of the two-dimensional pre-cracked square plate with an initial crack from the mid of the left-hand side to the center of the plate. All nodes in a square of horizon size δ at the lower right and upper right corner are fixed in displacement in both directions. On the lower left and the upper left, an external force in y-direction is applied to all nodes within a rectangle of size $\delta \times 2\delta$. Adapted from [15].

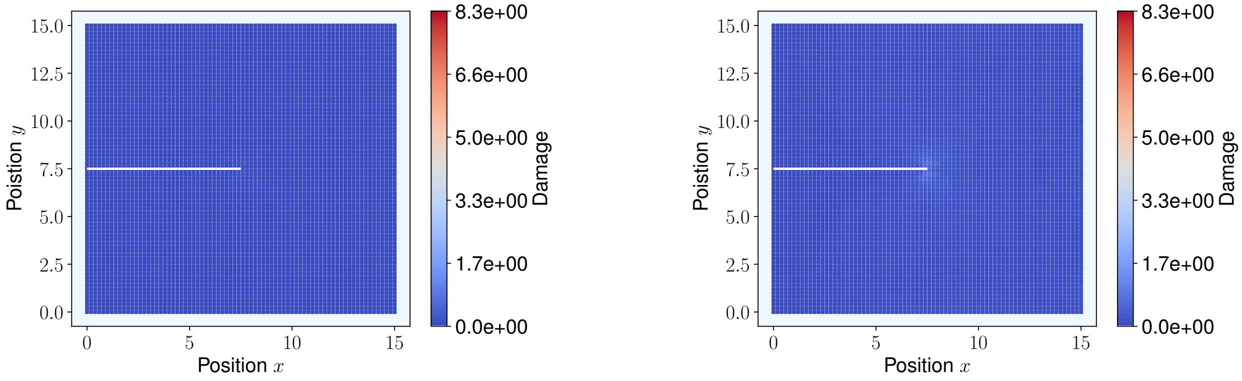

(a)

(b)

Figure 17: Plot of the damage for soft loading while the bond stretch is still in the linear regime and the material behaves linear elastic. The color map is chosen such that dark blue indicates no damage, light red indicates crack growth started, and dark red indicates that bonds are fully softened to zero. The damage after one load step (a) with $F_1 = \pm 4 \times 10^6$N some bonds are stretched up to 1.1% to the inflection point r^c before softening starts, and we can not see the damage yet. The damage after six load steps (b) with $F_6 = \pm 4 \times 10^6$N and the bonds are stretched around 7.2% close to the inflection point r^c, but are still in the linear regime. The damage is localized around the tip of the initial crack. Note that the damage is plotted with respect to the reference configuration D. The black line indicates the initial crack, and all bonds intersecting this line are initially broken.

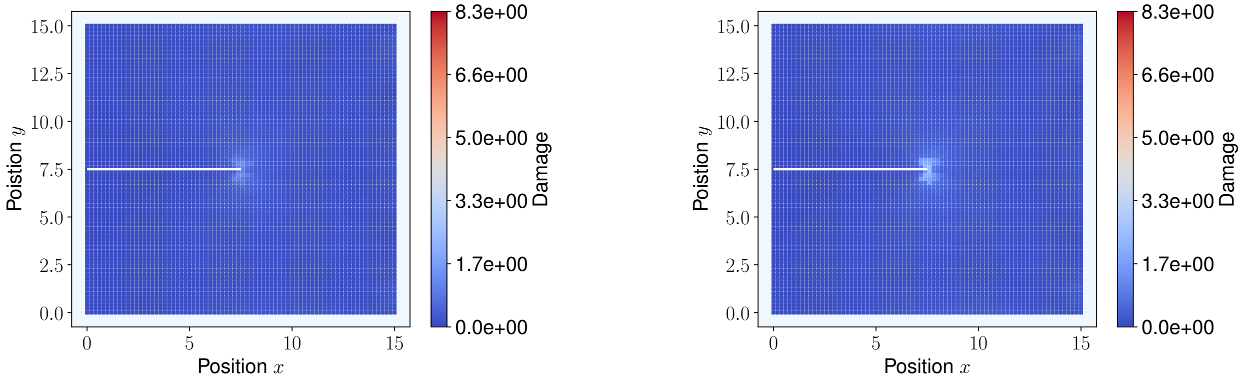

(a)

(b)

Figure 18: Plot of the damage for soft loading while the bond stretch started to soften, but the crack growth has not started yet. The color map is chosen such that dark blue indicates no damage, light red indicates crack growth started, and dark red indicates that bonds are fully softened to zero. The damage field after nine load steps (a) with $F_9 = 36 \times 10^6$N shows that first bond stretches are at 140% and exceeding the inflection point r^c and are softening. Here, the damage is still localized in a layer of horizon size δ at the tip of the initial crack. The damage after eleven load steps (b) with $F_{11} = 44 \times 10^6$N shows, that bonds are still softening, but crack growth has not yet begun. Note that the color is light blue and shortly turning to light red, which indicates crack growth. The damage is plotted with respect to the reference configuration D. The black line indicates the initial crack, and all bonds intersecting this line are initially broken.

shows, that the bonds are still softening, but crack growth has not yet begun. Note that the color is light blue and shortly turns to light red, which indicates crack growth.

Third, while the bond stretch is softening and unstable crack growth has begun. The crack is the location where the strength has been surpassed and softening begins. The simulation shows that the crack (indicated by the red zone) grows unstable with increasing load. The damage after twelve load steps with $F_{12} = 44.4$N is shown in (a) and after 21 load steps with $F_{21} = 44.436$N in (b), respectively. We had to reduce the load in force to $\pm 4 \times 10^5$N at load step 12 and further to $\pm 4 \times 10^3$N for the remaining load steps, since the large force resulted in an unstable matrix. At some point, the matrix kept unstable while decreasing the load further, which conforms with the theory that soft loading is

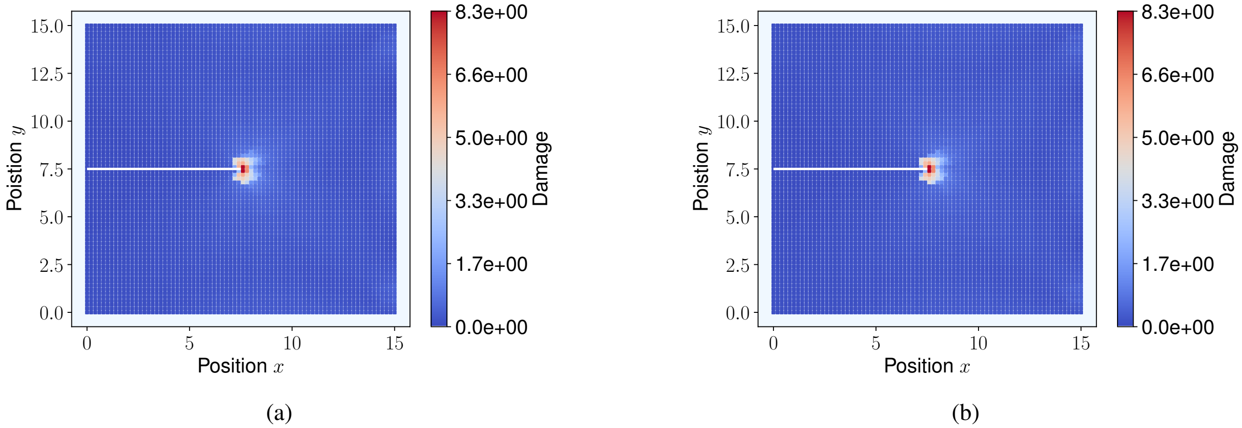

Figure 19: Damage for soft loading while the bond stretch is softening and unstable crack growth has begun. The crack is the location where the strength has been surpassed and softening begins. The simulation shows that the crack (indicated by the red zone) grows unstable with increasing load. The damage after twelve load steps with $F_{12} = 44.4\text{N}$ is shown in (a) and after 21 load steps with $F_{21} = 44.436\text{N}$ in (b), respectively. We had to reduce the load in force since the large force resulted in an unstable matrix. At some point, the matrix kept unstable while decreasing the load further, which conforms with the theory that soft loading is more likely to result in unstable crack growth. Note that the damage is plotted with respect to the reference configuration D. The white line indicates the initial crack, and all bonds intersecting this line are initially broken.

more likely to result in unstable crack growth. Figure 20 shows the corresponding displacement field in y-directions at the discrete PD nodes (black = $min(u_y)$ and gray = $max(u_y)$).

We like to share three remarks here. First, from the numerical perspective this behavior is seen in other quasi-static PD methods that once the crack starts to grow and bonds soften or drop to zero, the load step needs to be reduced to keep the condition number $con(K)$ of the tangent stiffness matrix feasible and the matrix solvable, see Figure 12. Second, from the physical perspective we know that once the crack starts to grow, the force gets less with the length of the crack to drive the crack. Thus, with the same force, the crack grows faster. Third, applying the load in force, the so-called soft loading, results that the crack only grows for few load steps and becomes unstable. The simulations show that this is to be expected since for the soft loading most of the deformation is borne by the pre-crack opening displacement with very small strain seen in the intact material except at the tip of the precrack where material damage and strain is concentrated. This behavior of unstable crack growth is reflected in the theory as depicted in the R curve in Figure 1. Once a load that intersects the R curve tangentially is reached, for example P_3 in Figure 1, the crack growth will remain unstable while increasing the load in force. However, one can find some smaller loads in force, for example P_1 and P_2, where the crack would grow for a small length l. For more details about soft loading and R curves, we refer to [3].

6.2.4 Pre-cracked plate with hard loading

For the hard loading, the geometry of the precracked square plate in Figure 16 was modified to apply the load in displacement to the top and bottom of the plate accordingly to Algorithm 4. Figure 21a shows the modified geometry for the hard loading. To the blue nodes, a positive load in displacement u and to the red nodes, a negative load in displacement $-u$ is applied. The lower and upper node of the last line of nodes are clamped to ensure a solvable / invertible tangent stiffness matrix. In that example, the maximal load of $\pm 6.9 \times 10^{-2}$ was applied to the lower and upper line of nodes, except the last clamped node. For the prescribed displacement field, $\mathbf{w}$ this maximal value decayed to 1×10^{-3} to the center of the plate. Due to numerical artifacts in the solver, the prescribed displacement should not be exactly zero at the center of the plate. Figure 21b shows the prescribed displacement field $\mathbf{w}$ at the first load step and for all successive load steps, the field increased linearly. All simulation parameters and material properties from the soft loading example were used, except the horizon ϵ was increased by a factor of two and $\epsilon = 8h$.

Figure 22 shows the damage field while the bond stretch S is less than one, which means that all bonds are still in the linear regime. Note that the damage is plotted with respect to the reference configuration D and the discrete nodes in the extended domains $D^{+\epsilon}$ and $D^{-\epsilon}$ are not shown. The black line indicates the initial crack. The color map is chosen such that dark blue indicates no damage, light red indicates crack growth started, and dark red indicates that the bonds are fully softened to zero. Figure 22a shows the damage field after the first load step, and we see that some

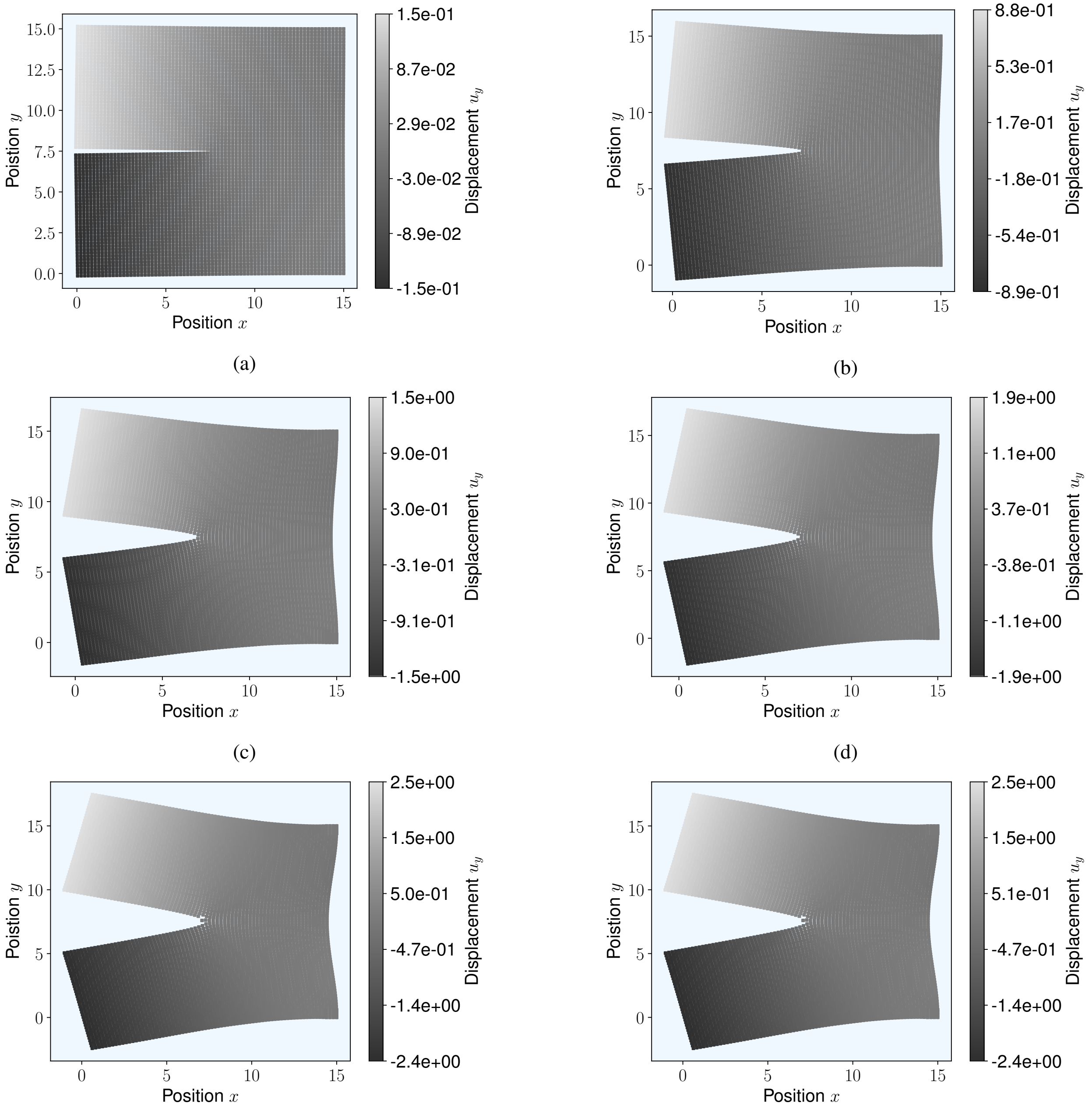

(a) (b)

(c) (d)

(e) (f)

Figure 20: Displacement u_y for soft loading at the discrete PD nodes (black = $min(u_y)$ and gray = $max(u_y)$) for the following loading steps: A external force $F_1 = \pm 4 \times 10^6$N was applied for one load step (a), after six load steps (b), after nine load steps (a), and 11 load steps b. An external force $F_2 = \pm 4 \times 10^5$N was applied for one load step a since the larger load resulted in an unstable matrix. After that, an external force $F_3 = \pm 4 \times 10^3$N was applied for nine time steps (b) before the matrix got unstable again.

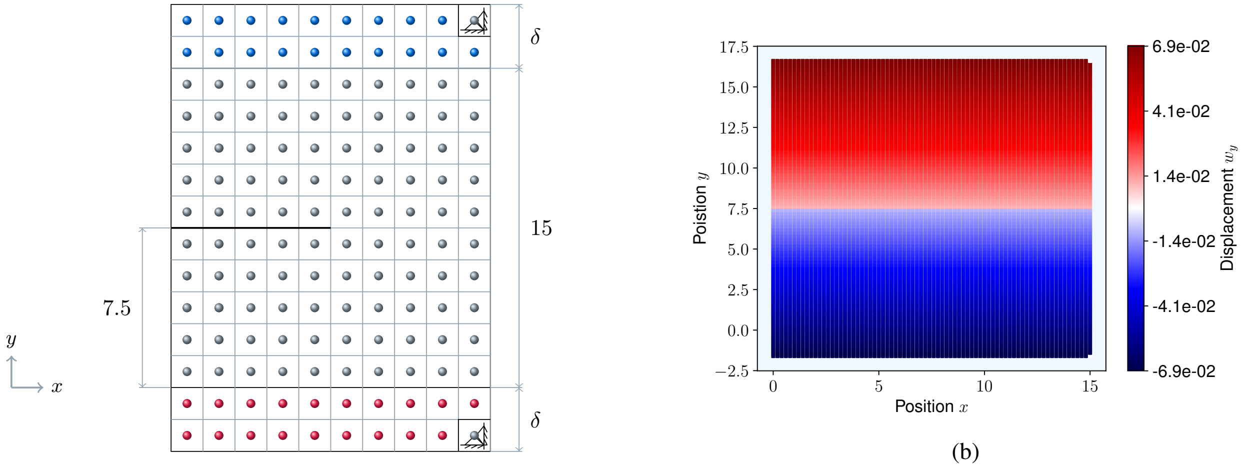

(a)

(b)

Figure 21: Extended domain for the hard loading: (a) of the extended domain where a load in positive displacement $\boldsymbol{u}$ is applied to the blue colored discrete nodes and a negative load $\boldsymbol{u}$ in displacement to the red colored discrete nodes. (b) shows the field of the prescribed displacement $\boldsymbol{w}_y$ in the y-direction. For more details, we refer to Algorithm 4.

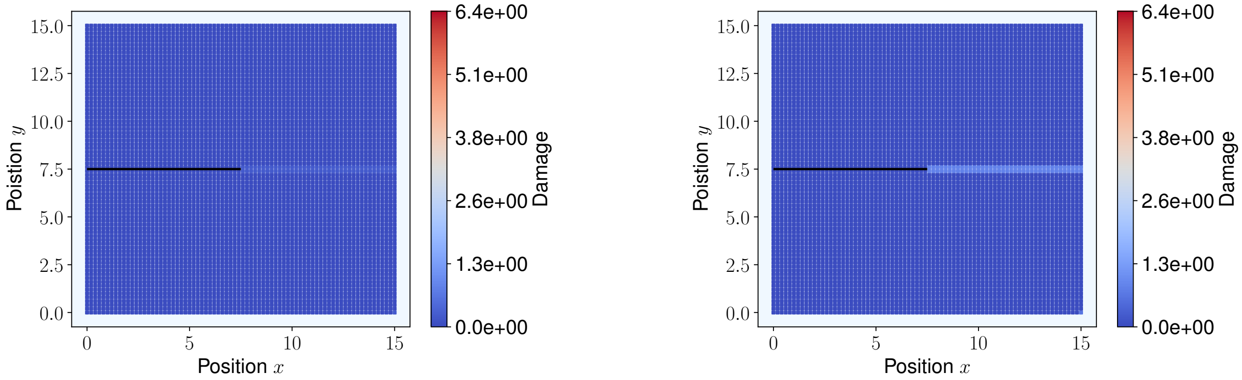

(a)

(b)

Figure 22: Plot of the damage for hard loading while the bond stretch is still in the linear regime and the material behaves linear elastic. The color map is chosen such that dark blue indicates no damage, light red indicates crack growth started, and dark red indicates that bonds are fully softened to zero. The damage after one load step (a) is localized around the center of the plate from the initial crack to the boundary. These bonds are stretched around 21% close to the critical inflection point r^c before the bond softening starts. After five load steps (b) the bonds are stretched around 82% close to the inflection point r^c, but are still in the linear regime. Since we still are in the linear regime, we see that the damage is equally distributed. Note that the damage is plotted with respect to the reference configuration D and the discrete nodes in the extended domains $D^{+\epsilon}$ and $D^{-\epsilon}$ are not shown. The black line indicates the initial crack, and all bonds intersecting this line are initially broken.

bonds close to the center of the plate are stretched around 21% close to the critical inflection point r^c before the bond softening starts. Since we pull with the same constant displacement at the top and bottom, we expect that the stretch is equally distributed at the beginning. In Figure 22b the damage field after five load steps is shown. Here, the bonds are stretched around 82% close to the inflection point r^c, but are still in the linear regime. Since we still are in the linear regime, we see that the damage is equally distributed.

Figure 23 shows the damage field once the bond softening started, but the crack has not started to grow yet. Figure 23a shows the damage field after seven load steps and the first bonds reached the inflection point r^C meaning the softening of bonds started, and we left the linear regime. However, crack growth has not yet initiated. Figure 23b shows the damage field were bonds stretched over 190% of the inflection point and the crack growth is close to initiate. Note that the color is light blue and shortly turns to light red, which indicates crack growth.

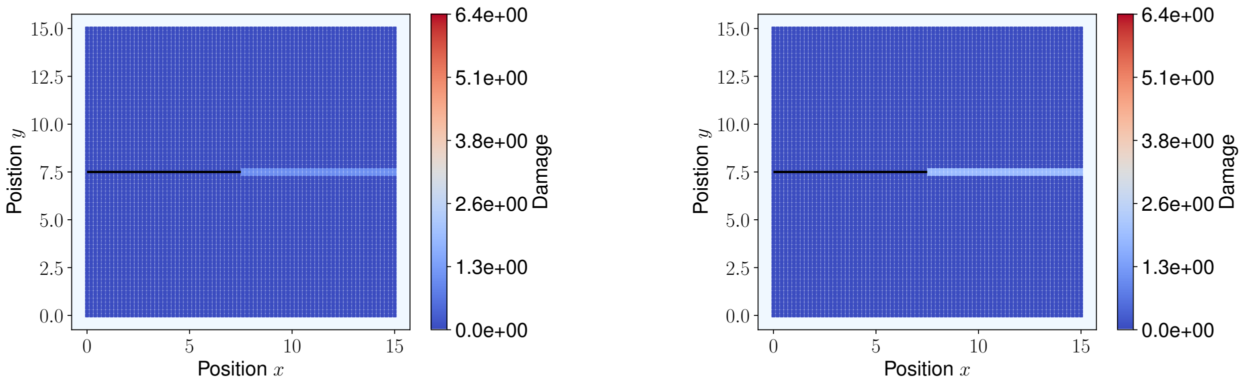

(a)

(b)

Figure 23: Plot of the damage for hard loading while the bond stretch started to soften, but the crack growth has not started yet. The color map is chosen such that dark blue indicates no damage, light red indicates crack growth started, and dark red indicates that bonds are fully softened to zero. The damage field after seven load steps (a) shows that first bond stretches are exactly at the inflection point r^c and close before softening. Here, the damage is still localized since we are still in the linear regime. The damage after nine load steps (b) shows, that bonds are stretched over 190$\%$ of the inflection point and the crack growth is close to initiate. Note that the color is light blue and shortly turning to light red, which indicates crack growth. The damage is plotted with respect to the reference configuration D and the discrete nodes in the extended domains $D^{+\epsilon}$ and $D^{-\epsilon}$ are not shown. The black line indicates the initial crack, and all bonds intersecting this line are initially broken.

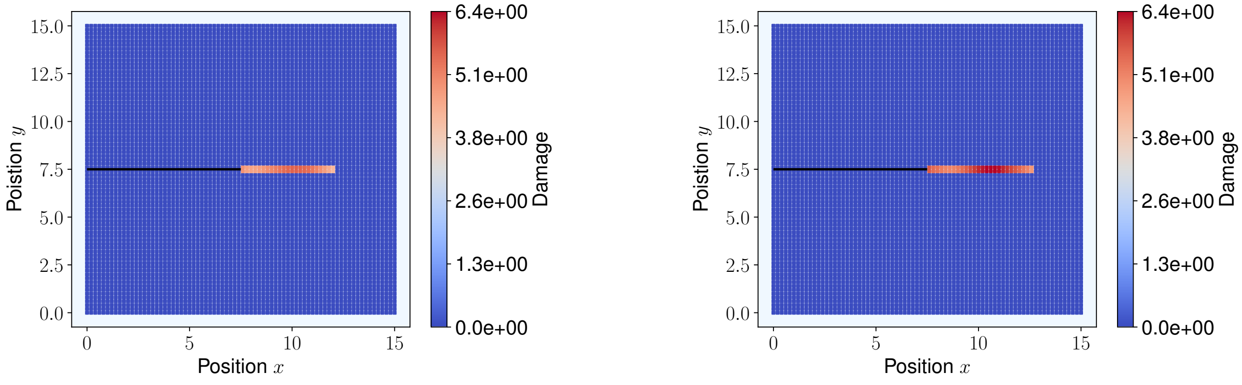

(a)

(b)

Figure 24: Plot of the damage for hard loading while the bond stretch is softening and stable crack growth has begun. The crack is the location where the strength has been surpassed and softening begins. The simulation shows that the crack (indicated by the red zone) grows stably with increasing load. The damage after 11 load steps is shown in (a) and after 12 load steps in (b), respectively. Note that the damage is plotted with respect to the reference configuration D and the discrete nodes in the extended domains $D^{+\epsilon}$ and $D^{-\epsilon}$ are not shown. The black line indicates the initial crack, and all bonds intersecting this line are initially broken.

Finally, Figure 24 shows crack growth. The simulation shows that the crack (indicated by the red zone) grows stably with increasing load. The damage after 11 load steps is shown in (a) and after 12 load steps in (b), respectively. The simulations again show that this is to be expected since for the hard loading the pre-crack opening displacement is small and the strain is now distributed uniformly within the intact material and stable crack growth can proceed. This is corroborated by the theory, recall Figure 1 where an example R curve with respect to the crack length is plotted. The dotted lines U_1 to U_5 sketch load in displacement. We see that these dotted lines intersect the R curve in normal direction, which indicates that the load in displacement needs to be increased to develop the crack further. This leads to Equation 1 and the crack growth tends to be more stable as in soft loading. For more details about soft loading and R curves, we refer to [3].

7 Conclusion

We showed the analytic derivation of the tangent stiffness matrix for a regularized nonlinear pairwise (RNP) potential. First, we validated our approach against solutions from classical continuum mechanics for linear elasticity to validate the linear regime of the RNP potential. In addition, we validated our approach against to a state-based model that uses the standard numerical derivations for assembling the stiffness matrix. Both validations showed good agreement for the validation of the linear regime without any damage. Furthermore, we could observe that the computational time of our approach was faster due to the reduced cost in the assembly of the tangent stiffness matrix. However, the Newton iterations per load step do not differ much. Second, the effect of softening bonds to the condition number of the tangent stiffness matrix $con(K)$ was investigated. Note that the crack growth was controlled by the user for this example. For a pre-crack square plate, the condition number increases linear with respect to the softening bonds. However, the crack should not grow faster than one or one and a half mesh width per load step to keep the condition number small. Third, fracture simulations for a ASTM E8 like tension test and a pre-crack square plate were obtained for soft loading. Here, both simulations resulted in unstable crack growth as intended for soft loading. However, for the hard loading, we could show stable crack growth closely to the boundary. Again, the novelty of our approach is that we soften the bonds and do not break them, which allows us analytic derivation of the analytic stiffness matrix.

To follow up on the proof of concept, the authors will implement the approach in their massive parallel C++ code to run larger simulations, which are needed for validation with experimental results and simulating more complex structures. Another aspect is to apply the method to three-dimensional structures. In addition, adaptive load steps are needed if one load step results in an unstable tangent stiffness matrix. Here, the authors like to investigate a more sophisticated choice of the reduced load steps based on numerical estimates or physical properties. Another aspect is to speed up the assembly of the stiffness matrix using the Fire algorithm [6] or Broyden-Fletcher–Goldfarb-Shanno (BFGS) [71] approach. A further challenge is to conduct a rigorous computational performance study of proposed methods to compare the reductions in computational cost. Here, all methods would need to run on the same computer hardware and one benchmark example would need to be defined for comparison. From the modeling aspect, the authors intend to apply the same numerical approach to the state-based RNP model [45] which includes dilatation forces.

Acknowledgments

This work was partly funded by DTIC Contract FA8075-14-D-0002/0007 and the Center of Computation & Technology at Louisiana State University. This material is based upon work supported by the U. S. Army Research Laboratory and the U. S. Army Research Office under contract/grant W911NF1610456 and the MURI Predicting and Controlling the Response of Particulate Systems through Grain-Scale Engineering - Cal-tech Prime W911NF1910245.

Financial disclosure

None reported.

Conflict of interest

The authors declare no potential conflict of interests.

Supporting information

The Python prototype of the implementation is available on GitHub[1] or on Zenodo [19]. Following Python packages were utilized: using numpy [54, 67], scipy [68], shapely, and matplotlib [33].

References

[1] Burak Aksoylu, Fatih Celiker, and Orsan Kilicer. Nonlocal operators with local boundary conditions in higher dimensions. *Advances in Computational Mathematics*, 45(1):453–492, 2019.

[2] WE Amoldi. The principle of minimized iteration in the solution of the matrix eigenvafue problem, quart. a&. *J. Appl. Math*, 9:17–29, 1951.

[1] `https://github.com/diehlpk/AnalyticStiffnessPython`

[3] Ted L Anderson. *Fracture mechanics: fundamentals and applications*. CRC press, 2017.

[4] ASTM International. ASTM E8-99 Standard test methods for tension testing of metallic materials. `https://www.astm.org/Standards/E8.htm`, 2001.

[5] ASTM International. ASTM E561-20 Standard Test Method for KR Curve Determination. `http://www.astm.org/cgi-bin/resolver.cgi?E561`, 2020.

[6] Erik Bitzek, Pekka Koskinen, Franz Gähler, Michael Moseler, and Peter Gumbsch. Structural relaxation made simple. *Physical review letters*, 97(17):170201, 2006.

[7] Michael Breitenfeld. *Quasi-static non-ordinary state-based peridynamics for the modeling of 3D fracture*. PhD thesis, University of Illinois at Urbana-Champaign, Champaign, IL, 2014.

[8] Michael D Brothers, John T Foster, and Harry R Millwater. A comparison of different methods for calculating tangent-stiffness matrices in a massively parallel computational peridynamics code. *Computer Methods in Applied Mechanics and Engineering*, 279:247–267, 2014.

[9] AC Cassell and RE Hobbs. Numerical stability of dynamic relaxation analysis of non-linear structures. *International Journal for numerical methods in engineering*, 10(6):1407–1410, 1976.

[10] Xi Chen and Max Gunzburger. Continuous and discontinuous finite element methods for a peridynamics model of mechanics. *Computer Methods in Applied Mechanics and Engineering*, 200(9-12):1237–1250, 2011.

[11] RH Dean and JW Hutchinson. Quasi-static steady crack growth in small-scale yielding. In *Fracture Mechanics*. ASTM International, 1980.

[12] P Diehl, R Lipton, and MA Schweitzer. Numerical verification of a bond-based softening peridynamic model for small displacements: deducing material parameters from classical linear theory. *INS Preprint No. 1630*, 2016.

[13] Patrick Diehl. Astm e8. Figshare, Nov 2020.

[14] Patrick Diehl. Emu-nodal discretization. Figshare, May 2020.

[15] Patrick Diehl. Pre-cracked square plate. Figshare, Nov 2020.

[16] Patrick Diehl. Validation 2d. Figshare, Jul 2020.

[17] Patrick Diehl. Validation of a one-dimensional bar. Figshare, 5 2020.

[18] Patrick Diehl. Displacement field for the two-dimensional benchmark. 10.6084/m9.figshare.15113508.v1, Aug 2021.

[19] Patrick Diehl. Quasistatic Fracture using Nonliner-Nonlocal Elastostatics with Explicit Tangent Stiffness Matrix. https://doi.org/10.5281/zenodo.5484312, September 2021.

[20] Patrick Diehl, Prashant K. Jha, Hartmut Kaiser, Robert Lipton, and Martin Lévesque. An asynchronous and task-based implementation of peridynamics utilizing hpx—the c++ standard library for parallelism and concurrency. *SN Applied Sciences*, 2(12):2144, Dec 2020.

[21] Patrick Diehl, Robert Lipton, Thomas Wick, and Mayank Tyagi. A comparative review of peridynamics and phase-field models for engineering fracture mechanics. *engrXiv*, 2021.

[22] Patrick Diehl, Serge Prudhomme, and Martin Lévesque. A review of benchmark experiments for the validation of peridynamics models. *Journal of Peridynamics and Nonlocal Modeling*, 1(1):14–35, 2019.

[23] Qiang Du. Nonlocal calculus of variations and well-posedness of peridynamics. In *Handbook of peridynamic modeling*, pages 101–124. Chapman and Hall/CRC, 2016.

[24] Etienne Emmrich and Olaf Weckner. The peridynamic equation and its spatial discretisation. *Mathematical Modelling and Analysis*, 12(1):17–27, 2007.

[25] Andris Freimanis and Ainars Paeglitis. Mesh sensitivity in peridynamic quasi-static simulations. *Procedia Engineering*, 172:284–291, 2017.

[26] Alan Arnold Griffith. Vi. the phenomena of rupture and flow in solids. *Philosophical transactions of the royal society of london. Series A, containing papers of a mathematical or physical character*, 221(582-593):163–198, 1921.

[27] Xin Gu, Erdogan Madenci, and Qing Zhang. Revisit of non-ordinary state-based peridynamics. *Engineering fracture mechanics*, 190:31–52, 2018.

[28] Max Gunzburger and Richard B Lehoucq. A nonlocal vector calculus with application to nonlocal boundary value problems. *Multiscale Modeling & Simulation*, 8(5):1581–1598, 2010.

[29] C Gurney and J Hunt. Quasi-static crack propagation. *Proceedings of the Royal Society of London. Series A. Mathematical and Physical Sciences*, 299(1459):508–524, 1967.

[30] Yile Hu, Hailong Chen, Benjamin W Spencer, and Erdogan Madenci. Thermomechanical peridynamic analysis with irregular non-uniform domain discretization. *Engineering Fracture Mechanics*, 197:92–113, 2018.

[31] YL Hu and Erdogan Madenci. Bond-based peridynamic modeling of composite laminates with arbitrary fiber orientation and stacking sequence. *Composite structures*, 153:139–175, 2016.

[32] Dan Huang, Guangda Lu, and Pizhong Qiao. An improved peridynamic approach for quasi-static elastic deformation and brittle fracture analysis. *International Journal of Mechanical Sciences*, 94:111–122, 2015.

[33] J. D. Hunter. Matplotlib: A 2d graphics environment. *Computing in Science & Engineering*, 9(3):90–95, 2007.

[34] Siavash Jafarzadeh, Farzaneh Mousavi, Adam Larios, and Florin Bobaru. A general and fast convolution-based method for peridynamics: applications to elasticity and brittle fracture. 2021.

[35] Siavash Jafarzadeh, Longzhen Wang, Adam Larios, and Florin Bobaru. A fast convolution-based method for peridynamic transient diffusion in arbitrary domains. *Computer Methods in Applied Mechanics and Engineering*, 375:113633, 2021.

[36] Prashant K. Jha and Robert Lipton. Numerical analysis of nonlocal fracture models in hölder space. *SIAM Journal on Numerical Analysis*, 56(2):906–941, 2018.

[37] Prashant K Jha and Robert Lipton. Numerical convergence of nonlinear nonlocal continuum models to local elastodynamics. *International Journal for Numerical Methods in Engineering*, 114(13):1389–1410, 2018.

[38] Prashant K Jha and Robert Lipton. Kinetic relations and local energy balance for lefm from a nonlocal peridynamic model. *International Journal of Fracture*, 226(1):81–95, 2020.

[39] B Kilic and Erdogan Madenci. An adaptive dynamic relaxation method for quasi-static simulations using the peridynamic theory. *Theoretical and Applied Fracture Mechanics*, 53(3):194–204, 2010.

[40] David C Lay, Steven R Lay, and Judi J McDonald. *Linear algebra and its applications*. Pearson, 2016.

[41] Robert Lipton. Dynamic brittle fracture as a small horizon limit of peridynamics. *Journal of Elasticity*, 117(1):21–50, 2014.

[42] Robert Lipton. Cohesive dynamics and brittle fracture. *Journal of Elasticity*, 124(2):143–191, 2016.

[43] Robert Lipton and Prashant K. Jha. Nonlocal elastodynamics and fracture. *Nonlinear Differ. Equ. Appl.*, 28(23), 2021.

[44] Robert Lipton, Richard B Lehoucq, and Prashant K Jha. Complex fracture nucleation and evolution with nonlocal elastodynamics. *Journal of Peridynamics and Nonlocal Modeling*, 133(1):122–130, 2019.

[45] Robert Lipton, Eyad Said, and Prashant K Jha. Dynamic brittle fracture from nonlocal double-well potentials: A state-based model. *Handbook of Nonlocal Continuum Mechanics for Materials and Structures*, pages 1–27, 2018.

[46] Robert Lipton, Eyad Said, and Prashant K Jha. Free damage propagation with memory. *Journal of Elasticity*, 133:129–153, 2018.

[47] Robert Lipton, Stewart Silling, and Richard Lehoucq. Complex fracture nucleation and evolution with nonlocal elastodynamics. *arXiv preprint arXiv:1602.00247*, 2016.

[48] David Littlewood. Roadmap for software implementation. In *Handbook of Peridynamic Modeling*, pages 147–178. Chapman and Hall/CRC, 2016.

[49] James N Lyness and Cleve B Moler. Numerical differentiation of analytic functions. *SIAM Journal on Numerical Analysis*, 4(2):202–210, 1967.

[50] JN Lyness. Differentiation formulas for analytic functions. *Mathematics of Computation*, pages 352–362, 1968.

[51] Richard W Macek and Stewart A Silling. Peridynamics via finite element analysis. *Finite Elements in Analysis and Design*, 43(15):1169–1178, 2007.

[52] Erdogan Madenci, Mehmet Dorduncu, Atila Barut, and Nam Phan. Weak form of peridynamics for nonlocal essential and natural boundary conditions. *Computer Methods in Applied Mechanics and Engineering*, 337:598–631, 2018.

[53] Yozo Mikata. Analytical solutions of peristatic and peridynamic problems for a 1d infinite rod. *International Journal of Solids and Structures*, 49(21):2887–2897, 2012.

[54] Travis E Oliphant. *A guide to NumPy*, volume 1. Trelgol Publishing USA, 2006.

[55] Naveen Prakash and Ross J Stewart. A multi-threaded method to assemble a sparse stiffness matrix for quasi-static solutions of linearized bond-based peridynamics. *Journal of Peridynamics and Nonlocal Modeling*, pages 1–35, 2020.

[56] Serge Prudhomme and Patrick Diehl. On the treatment of boundary conditions for bond-based peridynamic models. *Computer Methods in Applied Mechanics and Engineering*, 372:113391, 2020.

[57] Timon Rabczuk and Huilong Ren. A peridynamics formulation for quasi-static fracture and contact in rock. *Engineering Geology*, 225:42–48, 2017.

[58] JR Rice. Thermodynamics of the quasi-static growth of griffith cracks. *Journal of the Mechanics and Physics of Solids*, 26(2):61–78, 1978.

[59] Youcef Saad and Martin H Schultz. Gmres: A generalized minimal residual algorithm for solving nonsymmetric linear systems. *SIAM Journal on scientific and statistical computing*, 7(3):856–869, 1986.

[60] Yousef Saad. Krylov subspace methods for solving large unsymmetric linear systems. *Mathematics of computation*, 37(155):105–126, 1981.

[61] Martin H Sadd. *Elasticity: theory, applications, and numerics*. Academic Press, 2009.

[62] Yoshinori SHIIHARA, Shoki TANAKA, and Nobuhiro YOSHIKAWA. Fast quasi-implicit nosb peridynamic simulation based on fire algorithm. *Mechanical Engineering Journal*, 6(3):18–00363, 2019.

[63] Stewart A Silling. Reformulation of elasticity theory for discontinuities and long-range forces. *Journal of the Mechanics and Physics of Solids*, 48(1):175–209, 2000.

[64] Stewart A Silling and Ebrahim Askari. A meshfree method based on the peridynamic model of solid mechanics. *Computers & structures*, 83(17-18):1526–1535, 2005.

[65] Stewart A Silling, M Epton, O Weckner, Ji Xu, and E23481501120 Askari. Peridynamic states and constitutive modeling. *Journal of Elasticity*, 88(2):151–184, 2007.

[66] BHV Topping and AI Khan. Parallel computation schemes for dynamic relaxation. *Engineering computations*, 11(6):513–548, 1994.

[67] S. van der Walt, S. C. Colbert, and G. Varoquaux. The numpy array: A structure for efficient numerical computation. *Computing in Science Engineering*, 13(2):22–30, 2011.

[68] Pauli Virtanen, Ralf Gommers, Travis E. Oliphant, Matt Haberland, Tyler Reddy, David Cournapeau, Evgeni Burovski, Pearu Peterson, Warren Weckesser, Jonathan Bright, Stéfan J. van der Walt, Matthew Brett, Joshua Wilson, K. Jarrod Millman, Nikolay Mayorov, Andrew R. J. Nelson, Eric Jones, Robert Kern, Eric Larson, CJ Carey, İlhan Polat, Yu Feng, Eric W. Moore, Jake Vand erPlas, Denis Laxalde, Josef Perktold, Robert Cimrman, Ian Henriksen, E. A. Quintero, Charles R Harris, Anne M. Archibald, Antônio H. Ribeiro, Fabian Pedregosa, Paul van Mulbregt, and SciPy 1. 0 Contributors. SciPy 1.0: Fundamental Algorithms for Scientific Computing in Python. *Nature Methods*, 17:261–272, 2020.

[69] Fei Wang, Yu'e Ma, Yanning Guo, and Wei Huang. Studies on quasi-static and fatigue crack propagation behaviours in friction stir welded joints using peridynamic theory. *Advances in Materials Science and Engineering*, 2019, 2019.

[70] Hong Wang and Hao Tian. A fast galerkin method with efficient matrix assembly and storage for a peridynamic model. *Journal of Computational Physics*, 231(23):7730–7738, 2012.

[71] Jian-Ying Wu, Yuli Huang, and Vinh Phu Nguyen. On the bfgs monolithic algorithm for the unified phase field damage theory. *Computer Methods in Applied Mechanics and Engineering*, 360:112704, 2020.

[72] Mirco Zaccariotto, Fabio Luongo, U Galvanetto, et al. Examples of applications of the peridynamic theory to the solution of static equilibrium problems. *The Aeronautical Journal*, 119(1216):677–700, 2015.